



HAL
open science

Shear-induced migration in concentrated suspensions: particle mass conservation, contact pressure and jamming

Olivier Ozenda, Pierre Saramito, Guillaume Chambon

► **To cite this version:**

Olivier Ozenda, Pierre Saramito, Guillaume Chambon. Shear-induced migration in concentrated suspensions: particle mass conservation, contact pressure and jamming. *Journal of Non-Newtonian Fluid Mechanics*, 2022, 304, pp.104805. 10.1016/j.jnnfm.2022.104805 . hal-03331262v2

HAL Id: hal-03331262

<https://hal.science/hal-03331262v2>

Submitted on 26 Apr 2022

HAL is a multi-disciplinary open access archive for the deposit and dissemination of scientific research documents, whether they are published or not. The documents may come from teaching and research institutions in France or abroad, or from public or private research centers.

L'archive ouverte pluridisciplinaire **HAL**, est destinée au dépôt et à la diffusion de documents scientifiques de niveau recherche, publiés ou non, émanant des établissements d'enseignement et de recherche français ou étrangers, des laboratoires publics ou privés.

Shear-induced migration in concentrated suspensions: particle mass conservation, contact pressure and jamming

Olivier Ozenda^{a,b}, Pierre Saramito^{a,*}, Guillaume Chambon^b

^a*Lab. Jean Kuntzmann – CNRS and Université Grenoble-Alpes, F-38041 Grenoble, France*

^b*Univ. Grenoble-Alpes, INRAE, UR ETNA, F-38041 Grenoble, France*

Abstract

A two-velocity fluid model is presented to describe particle migration in mono-disperse suspensions of neutrally buoyant particles. In contrast to previous migration models, the proposed formulation allows us to impose explicit boundary conditions on particle velocity, and thereby to satisfy strict mass conservation for the particle phase. In addition, the upper bound on particle volume fraction (jamming limit) is strictly enforced through a non-smooth complementarity condition and the introduction of a particle jamming pressure. The model is applied to an axisymmetric Poiseuille flow and solved using a finite-element method. For that purpose, a specific, fully implicit algorithm based on non-smooth optimisation tools is developed and validated. Preliminary comparisons with experimental data from the literature show promising agreement. In particular, the model properly captures the formation of an inner plug region, in which the suspension is saturated and jammed.

Keywords: Suspension, Migration, Congested problem, Augmented Lagrangian method, Asymptotic expansion

1. Introduction

Last decade saw the introduction of granular concepts to describe the rheology and flow of suspensions of rigid particles [1, 2]. While hydro-dynamical effects are prominent in dilute mixtures, inter-particle contacts and friction start to play a role as soon as particle volume fraction ϕ exceeds values of 0.2–0.25, typically [3]. Contacts and friction, in particular, appear to be responsible for a number of specific rheological properties of concentrated suspensions, such as existence normal stress differences, particle pressure and micro structure

*Corresponding author

Email address: Pierre.Saramito@imag.fr (Pierre Saramito)

anisotropy [3, 4]. Contacts and friction can also lead to shear-thickening effects, and influence the value of the critical particle volume fraction ϕ_m above which the suspension is jammed and behaves as a solid [5, 6]. Various constitutive models have been proposed to describe these properties, either through phenomenological expressions of the particle stresses [7, 8, 6], inclusion of auxiliary conformation tensors related to micro structure evolution [9, 10, 11, 12, 13], or by explicitly accounting for granular processes [14, 15].

Among the specific properties of concentrated suspensions, shear-induced particle migration received a lot of attention since the seminal study of Leighton and Acrivos [16]. This process is responsible for the spontaneous development of particle volume fraction heterogeneities in sheared suspensions and can lead, for sufficiently large values of the average volume fraction, to the formation of jammed plugs in which ϕ reaches ϕ_m [17, 18]. While some recent approaches explore the direct numerical simulation of the fluid containing a discrete distribution of particles (see e.g. [19]), most numerical simulations of the migration process base on a continuous mathematical model for the fluid–particle mixture. Since the first phenomenological modelling attempt by Phillips et al. [20], various models based on two-phase mixture theory [21] have been proposed. Formulation of a closed system of conservation laws for a two-phase continuous medium requires closure assumptions to express the contributions of each phase to the Cauchy stress tensor of the mixture as well as the forces on the particle phase [22, 23]. Specific attention should be paid to the contribution of particles and contacts to stresses, as it is now clear that shear-induced migration is driven by the existence of normal stress gradients in the suspension [3, 4]. The classical *suspension balance model* (SBM), which is based on empirical expressions for the particle stress and inter-phase drag, expresses, in absence of inertia, as a closed system of equations for the mixture velocity and particle volume fraction [24, 7]. Qualitatively, this model proved successful in capturing migration effects in different flow configurations [25, 8]. However, difficulties arise when ϕ approaches the limit ϕ_m and the strain rate vanishes. In practice, these issues are usually dealt with by considering unrealistically large values of ϕ_m , and by adding an ad-hoc non-local term that effectively prevents the strain rate from vanishing [25]. As a consequence the model cannot capture the formation of truly jammed plugs. Note however that a recent extension of SBM, implementing a process of *inelastic compressibility* through which the particle volume fraction can increase beyond the limit ϕ_m in jammed regions, has been shown to overcome this limitation, and to effectively predict realistic plugs [15]. Physically, such solid compressibility of jammed regions can arise due to non-local effects and fluctuations induced by the neighbouring sheared regions [26, 15, 27]. Finally, another drawback of such single velocity models is the difficulty to impose proper conditions on the particle flux at the boundaries of the domain. As a consequence, conservation of particle mass might not always be satisfied in numerical implementations [25].

In this paper, we propose an alternative migration model that explicitly integrates the saturation of the mixture when the volume fraction reaches the limit

ϕ_m . A unilateral constraint is added to the system of conservation laws through a complementarity condition to ensure that ϕ remains effectively bounded by ϕ_m . In addition, the model is based on a two-velocity formulation, and embodies an explicit computation of the difference between the mixture velocity and the particle phase velocity (i.e. the migration velocity). Boundary conditions on the particle flux can be explicitly imposed, such that strict conservation of particle mass is satisfied. Since the study is primarily devoted to the formulation and numerical solution of the system of conservation laws, particle stress is modelled using the classical phenomenological constitutive relation proposed by Morris and Boulay [7]. Inter-particle friction or effects of micro structure are not directly taken into account at this stage, although they might be included in further versions of the model by using more sophisticated constitutive models [10, 15, 13]. As explained below, we do however introduce an additional pressure term that can be interpreted as a jamming pressure, to properly deal with the complementarity condition. Compared to SBM, our model also involves an additional inter-phase stress term required for the stability of the two-velocity formulation and to enforce boundary conditions on particle velocity.

From a mathematical standpoint, flow models involving a complementarity condition are usually referred to as *congested* problems [28, 29]. The mathematical properties of such systems were first studied by Lions and Masmoudi [30], and more recently by Bresch et al. [28]. Hyperbolic variants of these models, without diffusive terms, were first applied to road traffic [31, 32] using the asymptotic preserving numerical method [33]. Later, these models were also applied to crowd motion [34], granular media [35, 36], and shallow flows in cavities [37]. A general overview of hyperbolic systems with unilateral constraints was exposed by Bouchut et al. [38], and specific solutions were studied by Berthelin [39], Berthelin and Bouchut [40] and recently Chen and Zhai [41].

The paper is structured as follows. The proposed two-phase model for the mixture velocity, migration velocity and particle volume fraction is presented in section 2. Through an asymptotic analysis, a reduced system is then derived for the case of a uniform axisymmetric Poiseuille flow (flow in a circular tube). Section 3 proposes a numerical method to solve the model in the case of the Poiseuille problem, implementing a specific augmented Lagrangian approach to handle the nonlinearity associated with the complementarity condition. Spatial discretisation is performed using finite elements. Results are presented and discussed in section 4. After a careful investigation of the convergence properties of the numerical method, the physical characteristics of the solutions are described, and direct comparisons with experimental measurements of Oh et al. [18] are shown. Section 5 presents final discussions and conclusions.

notation	description	notation	description
\mathbf{u}	bulk velocity	ρ	fluid and particle density
\mathbf{w}	migration velocity	η_0	fluid viscosity
q	pipe flow rate	$\boldsymbol{\tau}_p$	particle stress tensor
p	mixture pressure	$Q = \text{diag}(1, \lambda_2, \lambda_3)$	normal stress tensor
p_j	jamming pressure	$s(\psi)$	hindrance function
ϕ	volume fraction	α	exponent in $s(\psi)$
ϕ_m	maximal volume fraction	K_n, K_s	reduced viscosities
$\psi = \phi/\phi_m$	reduced volume fraction	$\varepsilon = r_p/R$	dimensionless particle radius
Ω	flow domain	$Re = 2\rho q/(\pi R)$	Reynolds number
R	tube radius	h	mesh size
L	tube length	Δt	time step
T	final time	μ	augmentation parameter
r_p	particle radius		

Table 1: Notations used in the paper.

2. Migration model

2.1. Two velocity formulation

Let r_p be the radius of the rigid spherical particles, and η_0 be the viscosity of the interstitial Newtonian fluid. For the sake of simplicity, we assume here a neutral buoyancy: let ρ denote the constant mass density of both the fluid and the particles. This assumption is not fundamental, and the present theory could be extended to also include different mass densities and sedimentation effects. The dynamics of the mixture, at a continuous macroscopic scale, is described by two independent velocities. Without loss of generality, we choose as independent variables the velocity of the mixture, denoted by \mathbf{u} , and the velocity difference between the two phases, hereafter called *migration velocity*, denoted by \mathbf{w} . Note that $\mathbf{u} + \mathbf{w}$ represents the velocity of the particles phase.

The volume fraction is denoted by ϕ and is bounded by the maximal volume fraction ϕ_m . When $\phi = \phi_m$, the mixture is *jammed* and behaves as a solid. For convenience, the reduced volume fraction $\psi = \phi/\phi_m$ is introduced. The constraint $\phi \leq \phi_m$, or equivalently $\psi \leq 1$, can be expressed as a *linear complementarity problem* Cottle and Dantzig [42], Duvaut and Lions [43]:

$$0 \leq (1 - \psi) \perp p_j \geq 0 \Leftrightarrow \begin{cases} 1 - \psi & \geq 0 \\ p_j & \geq 0 \\ (1 - \psi)p_j & = 0 \end{cases} \quad (1)$$

Hence, the two quantities $1 - \psi$ and p_j should always be positive, and the \perp notation expresses that their product should also be zero. When $\psi < 1$, we then have $p_j = 0$, while p_j can be nonzero when $\psi = 1$ in the jammed case. This constraint expresses, at the macroscopic scale, the microscopic non-penetration

between the rigid particles when contacts occur. The quantity p_j is a Lagrange multiplier that can be interpreted as a *jamming pressure*. Note that (1) should be satisfied locally, as some regions of the flow can be jammed while others are not.

Table 1 summarises the main notations used in this paper. Let $\Omega \subset \mathbb{R}^d$ denote the flow domain, where $d \geq 1$ is the physical space dimension, and let $T > 0$ be the final time. The problem to solve writes:

(P): find \mathbf{u} , \mathbf{w} , p , ψ , p_j , defined in $]0, T[\times \Omega$, such that

$$\left\{ \begin{array}{l} \rho \left(\frac{\partial \mathbf{u}}{\partial t} + \mathbf{u} \cdot \nabla \mathbf{u} \right) - \mathbf{div} (-p \mathbf{I} + 2\eta_0 D(\mathbf{u}) + \boldsymbol{\tau}_p) = \mathbf{f} \text{ in }]0, T[\times \Omega \quad (2a) \\ \rho \phi_m \psi \left(\frac{\partial(\mathbf{u} + \mathbf{w})}{\partial t} + (\mathbf{u} + \mathbf{w}) \cdot \nabla(\mathbf{u} + \mathbf{w}) \right) - \mathbf{div} (-p_j \mathbf{I} + \boldsymbol{\tau}_p) \\ \quad + \frac{\eta_0 s(\psi)}{r_p^2} \mathbf{w} - \mathbf{div} (2\eta_0 s(\psi) D(\mathbf{w})) = 0 \text{ in }]0, T[\times \Omega \quad (2b) \\ \mathbf{div} \mathbf{u} = 0 \text{ in }]0, T[\times \Omega \quad (2c) \\ \frac{\partial \psi}{\partial t} + \mathbf{div} ((\mathbf{u} + \mathbf{w}) \psi) = 0 \text{ in }]0, T[\times \Omega \quad (2d) \\ 0 \leq (1 - \psi) \perp p_j \geq 0 \quad \text{in }]0, T[\times \Omega \quad (2e) \\ \boldsymbol{\tau}_p = 2\eta_0 \frac{\psi}{1 - \psi} \left(\frac{5\phi_m}{2} + \frac{\psi}{1 - \psi} K_s \right) D(\mathbf{u}) \\ \quad - 2\eta_0 \left(\frac{\psi}{1 - \psi} \right)^2 K_n |D(\mathbf{u})| Q \text{ in }]0, T[\times \Omega \quad (2f) \\ \mathbf{u} = \mathbf{u}_\Gamma \quad \text{and} \quad \mathbf{w} = \mathbf{w}_\Gamma \quad \text{in }]0, T[\times \partial\Omega \quad (2g) \\ \psi = \psi_\Gamma \quad \text{in }]0, T[\times \partial\Omega_- \quad (2h) \\ \mathbf{u}(t=0) = \mathbf{u}_0, \quad \mathbf{w}(t=0) = \mathbf{w}_0 \quad \text{and} \quad \psi(t=0) = \psi_0 \quad \text{in } \Omega \quad (2i) \end{array} \right.$$

Equations (2a) and (2c) express the momentum and mass conservation of the mixture, respectively, while Equations (2b) and (2d) express the momentum and mass conservation of the particle phase. Note that the latter has the form of an evolution equation for the reduced volume fraction ψ . Equation (2a) involves the expression of the Cauchy stress tensor of the mixture $\boldsymbol{\sigma}_m = -p \mathbf{I} + 2\eta_0 D(\mathbf{u}) + \boldsymbol{\tau}_p$, where $D(\mathbf{u}) = (\nabla \mathbf{u} + \nabla \mathbf{u}^T)/2$. The Lagrange multiplier p , that interprets as the bulk pressure, is introduced to enforce the mixture incompressibility constraint (2c). The quantity $\boldsymbol{\tau}_p$ represents the contribution of the particle phase to the extra-stress tensor, and will be discussed later. On the right-hand-side, \mathbf{f} represents any external body force. Equation (2b) involves the Cauchy stress of the particle phase $-p_j \mathbf{I} + \boldsymbol{\tau}_p$, where p_j is the jamming pressure related to the jamming constraint (2e), as explained above. Note that the particle pressure then expresses as $p_j - \text{tr}(\boldsymbol{\tau}_p)/3$. Equation (2b) also involves a net force exerted on the particle phase:

$$\frac{\eta_0 s(\psi)}{r_p^2} \mathbf{w} - \mathbf{div} (2\eta_0 s(\psi) D(\mathbf{w})).$$

The first term in this force corresponds to the drag force exerted by the fluid phase, where $s(\psi)$ is a *hindrance function* for which we use the following expression proposed by Miller and Morris [25]:

$$s(\psi) = \frac{9}{2(1 - \phi_m \psi)^{\alpha-1}(1 - \psi)},$$

with $\alpha \in [2, 5]$ a material parameter. As discussed by Miller and Morris [25], this expression is adapted from the classical Richardson–Zaki function, with an additional $(1 - \psi)$ factor in the denominator to enforce that migration ceases when maximum packing fraction is reached. The second term in the particle-phase force, namely $\text{div}(2\eta_0 s(\psi)D(\mathbf{w}))$, represents a second-order correction with respect to particle radius r_p . It is introduced here in order to allow for the imposition of boundary conditions on particle velocity $\mathbf{u} + \mathbf{w}$, or equivalently on \mathbf{w} (see Equation (2g)).

Equation (2f) is the phenomenological constitutive relation for the particle stress tensor $\boldsymbol{\tau}_p$ initially proposed by Morris and Boulay [7]. Constants K_s and K_n are material parameters that control the shear and normal viscosities, respectively. Note that the particle stress tensor $\boldsymbol{\tau}_p$ diverges when $\psi \rightarrow 1$, so that this constitutive model cannot be used as such in saturated regions. In what follows, a regularisation will be used to overcome this limitation (see section 3). The tensor Q expresses as $\text{diag}(1, \lambda_2, \lambda_3)$ in the velocity, gradient, vorticity basis associated to viscosimetric flows (see e.g. [44, p. 158]), where λ_2 and λ_3 are material parameters controlling the two normal stress differences. Expressions of Q adapted to the case of non-viscosimetric flows have also been proposed [45], but will not be used here.

Finally, the problem is closed by suitable initial and boundary conditions on velocities \mathbf{u} and \mathbf{w} and reduced volume fraction ψ , expressed by Equations (2g)–(2i). Here $\partial\Omega_-$ denotes the upstream boundary domain for the particle phase:

$$\partial\Omega_- = \{\mathbf{x} \in \partial\Omega \text{ such that } (\mathbf{u} + \mathbf{w})(\mathbf{x}) \cdot \mathbf{n}(\mathbf{x}) < 0\},$$

and \mathbf{u}_Γ , \mathbf{w}_Γ , ψ_Γ , \mathbf{u}_0 , \mathbf{w}_0 , ψ_0 , are given boundary and initial data satisfying $\text{div} \mathbf{u}_0 = 0$, $\int_{\partial\Omega} \mathbf{u}_\Gamma \, ds = 0$ and $\psi_0, \psi_\Gamma \in [0, 1]$. Observe that, from (2d) and since $\psi(t=0) \geq 0$, then $\psi(t) \geq 0$ for any $t \geq 0$.

Suspension balance model (SBM), which only involves the mixture velocity [25], can be recovered by neglecting inertial terms in equations (2a) and (2b), and omitting the complementarity condition (2e) as well as the term $\text{div}(-p_j \mathbf{I} + 2\eta_0 s(\psi)D(\mathbf{w}))$ in equation (2b). Note that, in SBM, the constraint $\psi \leq 1$ is not strictly imposed, but effectively verified through the addition of an ad-hoc non-local term to the particle stress tensor $\boldsymbol{\tau}_p$.

Appendix A further expands on the link between the present model and the general mixture theory developed by Jackson [46], including formal definitions of the variables in terms of fluid and solid phase averages. Let us also note that, as an alternative to the stress partition used in system (2), one could define

the *total* Cauchy stress tensor of the particle phase as $\boldsymbol{\sigma}_p = \boldsymbol{\tau}_p + \boldsymbol{\tau}_{p,nl} - p_j \mathbf{I}$, with $\boldsymbol{\tau}_{p,nl} = 2\eta_0 s(\psi) D(\mathbf{w})$. Physically, the new corrective term $\boldsymbol{\tau}_{p,nl}$ could then be interpreted as a non-local contribution to the particle stress in unjammed regions, in the same spirit as non-local rheological models proposed for granular materials and other complex fluids [47, 48]. The *total* particle pressure then expresses as $p_p = p_j - \text{tr}(\boldsymbol{\tau}_p + \boldsymbol{\tau}_{p,nl})/3$, also involving a contribution from $\boldsymbol{\tau}_{p,nl}$.

Finally, let us comment on the mathematical structure of problem (2a)-(2i). The pair (\mathbf{u}, p) satisfies an incompressible Navier-Stokes-like subsystem (2a), (2c), while the triplet (\mathbf{w}, ψ, p_j) satisfies a variable-density Navier-Stokes-like subsystem (2b), (2d), associated to condition (2e) that guarantees $\psi \in [0, 1]$. Coupling between the two subsystems is achieved by the tensor $\boldsymbol{\tau}_p$ that depends on \mathbf{u} and ψ from (2f).

2.2. Uniform Poiseuille flow

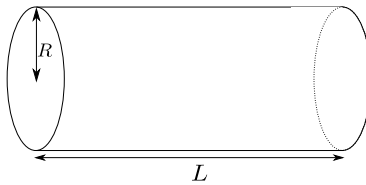


Figure 1: Circular tube geometry for the Poiseuille flow.

Let us consider here the circular tube geometry represented on Fig. 1, with L the length of the tube and R its radius. Let (r, θ, z) be the associated cylindrical coordinate system. We consider axisymmetric flows independent upon θ . The tube is assumed to be sufficiently long, i.e. $L \rightarrow \infty$, such that the flow is also considered to be independent upon z . Hence, mixture velocity writes $\mathbf{u}(t, r) = (0, 0, u_z(t, r))$, while migration velocity can develop a nonzero radial component and expresses as $\mathbf{w}(t, r) = (w_r(t, r), 0, w_z(t, r))$. The average reduced particle volume fraction ψ_0 is constant for $t \geq 0$, and we also consider that the mixture flow rate q is imposed and constant for $t > 0$.

An asymptotic analysis for $L \rightarrow \infty$, presented in [Appendix B](#), shows that problem (2a)-(2i) then reduces to, in dimensionless form:

(Q): find u_z, w_z, w_r, ψ, p_j , defined in $]0, T[\times]0, 1[$ and f_z in $]0, T[$, s.t.

$$\left\{ \begin{array}{l} Re \partial_t u_z - \frac{\partial_r}{r} (r \eta_{app}(\psi) \partial_r u_z) + f_z = 0 \text{ in }]0, T[\times]0, 1[\quad (3a) \\ Re \phi_m \psi \partial_t (u_z + w_z) + \frac{s(\psi)}{\varepsilon^2} w_z \\ \quad - \frac{\partial_r}{r} (r s(\psi) \partial_r w_z + r (\eta_{app}(\psi) - 1) \partial_r u_z) = 0 \text{ in }]0, T[\times]0, 1[\quad (3b) \\ Re \phi_m \psi \partial_t w_r + \frac{s(\psi)}{\varepsilon^2} w_r - \frac{\partial_r}{r} (2r s(\psi) \partial_r w_r) \\ \quad + \frac{\eta_{n,\theta}(\psi) |\partial_r u_z|}{r} - \frac{\partial_r}{r} (r \eta_{n,r}(\psi) |\partial_r u_z|) + \partial_r p_j = 0 \text{ in }]0, T[\times]0, 1[\quad (3c) \\ \partial_t \psi + \frac{\partial_r}{r} (r w_r \psi) = 0 \text{ in }]0, T[\times]0, 1[\quad (3d) \\ 0 \leq (1 - \psi) \perp p_j \geq 0 \text{ in }]0, T[\times]0, 1[\quad (3e) \\ \int_0^1 u_z(t, r) r dr = \frac{1}{4}, \quad \forall t \in]0, T[\quad (3f) \\ \partial_r u_z(t, r=0) = u_z(t, r=1) = 0, \quad \forall t \in]0, T[\quad (3g) \\ \partial_r w_z(t, r=0) = w_z(t, r=1) = 0, \quad \forall t \in]0, T[\quad (3h) \\ w_r(t, r=0) = w_r(t, r=1) = 0, \quad \forall t \in]0, T[\quad (3i) \\ u_z(t=0) = w_z(t=0) = w_r(t=0) = 0, \psi(t=0) = \psi_0 \text{ in }]0, 1[\quad (3j) \end{array} \right.$$

where $\varepsilon = r_p/R$ and $Re = \rho U R / \eta_0$, with $U = 2q/(\pi R^2)$ the characteristic velocity scale. Here, p_j denotes the Lagrange multiplier associated to the complementarity condition (3e). Similarly, f_z is a Lagrange multiplier associated to the mixture flow rate constraint (3f). Note that f_z interprets as the longitudinal gradient of mixture pressure. The rheological functions η_{app} , $\eta_{n,r}$ and $\eta_{n,\theta}$ involved are given by

$$\begin{aligned} \eta_{app}(\psi) &= 1 + \frac{5\phi_m}{2} \left(\frac{\psi}{1-\psi} \right) + K_s \left(\frac{\psi}{1-\psi} \right)^2 \\ \eta_{n,r}(\psi) &= -\alpha_{n,r} \left(\frac{\psi}{1-\psi} \right)^2 \\ \eta_{n,\theta}(\psi) &= -\alpha_{n,\theta} \left(\frac{\psi}{1-\psi} \right)^2 \end{aligned}$$

with $\alpha_{n,r} = \lambda_2 K_n$ and $\alpha_{n,\theta} = \lambda_3 K_n$. With these notations, the dimensionless particle stress tensor expresses as:

$$\boldsymbol{\tau}_p = \begin{pmatrix} \eta_{n,r}(\psi) |\partial_r u_z| & 0 & (\eta_{app}(\psi) - 1) \partial_r u_z \\ 0 & \eta_{n,\theta}(\psi) |\partial_r u_z| & 0 \\ (\eta_{app}(\psi) - 1) \partial_r u_z & 0 & \eta_{n,z}(\psi) |\partial_r u_z| \end{pmatrix} \quad (4)$$

Finally, note that, unlike for 2D plane channel flow [15], particle normal stress differences are explicitly involved in the circular tube flow considered here.

Let us observe the mathematical structure of problem (3a)-(3j). Relations (3a) and (3f) constitute a linear constrained parabolic sub-problem for the unknown u_z and the Lagrange multiplier f_z , where ψ is considered as known. This first linear sub-problem is closed by boundary and initial conditions (3g) and (3j) for u_z . Similarly, relation (3b) constitute a second linear parabolic sub-problem for the unknown w_z , where both u_z and ψ are considered as known. This second linear sub-problem is closed with boundary and initial conditions (3h) and (3j) for w_z . Finally, relations (3c), (3d) and (3e) constitute a nonlinear constrained sub-problem for the unknowns w_r and ψ and the Lagrange multiplier p_j , where u_z is considered as known. This problem will henceforth be called the congested flow sub-problem. This third nonlinear sub-problem is closed with boundary and initial conditions (3i) and (3j) for w_r and ψ . The Lagrange multiplier p_j that imposes the nonlinear constraint $\psi \leq 1$ in (3e) acts on w_r via its evolution equation (3c). Then, ψ is convected by w_r in accordance with the mass conservation equation (3d). Hence, p_j acts as a subtle indirect control upon ψ via w_r . The numerical solution of the problem presented in the following section is mainly suggested by observation of this mathematical structure.

3. Numerical resolution

We present in this section a fully implicit algorithm for the numerical resolution of problem (Q) (uniform Poiseuille flow). At each time step of an outer loop, the three sub-problems outlined above are solved, and a fixed point inner loop ensures the convergence. Note that, unlike Degond et al. [33] and Degond and Tang [49] who solved an hyperbolic congested flow problem with an explicit time scheme, we choose here an implicit time discretisation to avoid restrictions on time steps due to stability criteria. As the present problem also involves viscous and diffusion terms, such conditions on time step would be too restrictive. Particle migration tends to be a slow process, for which the use of large time steps is required.

Presentation of the numerical algorithm is organised as follows. Subsection 3.1 describes the fixed point method that splits problem (Q) into the three associated sub-problems. Two of these sub-problems, namely (S_1) and (S_2), are linear and provide computations of (u_z, f_z) and w_z , respectively. The three other unknowns, w_r, p_j, ψ , are solution of a non smooth optimisation problem (S_3). Problem (S_3), which implements a complementarity condition between p_j and ψ , cannot be solved by classical optimisation algorithms. This problem is thus approached by another problem (\tilde{S}_3), implementing a complementarity condition between p_j and $\partial_r w_r / r$. An optimisation method to solve problem (\tilde{S}_3) is presented in subsection 3.2. A corrective term is added to the cost function to apply an augmented Lagrangian method. The solution of (\tilde{S}_3) then expresses as a critical point of the augmented cost function, and is found using an Uzawa algorithm. Finally, subsection 3.3 describes the spatial discretisation used.

3.1. Implicit time discretisation

Let $\Delta t > 0$ be the time step and $t_n = n\Delta t$, $n \in \mathbb{N}$, be the discrete times. A sequence of semi-discrete in time solutions $\left(u_z^{(n)}, w_z^{(n)}, w_r^{(n)}, \psi^{(n)}, f_z^{(n)}, p_j^{(n)}\right)_{n \geq 0}$ is defined by recurrence. When $n = 0$, the solution is provided by the initial conditions, $u_z^{(0)} = w_z^{(0)} = w_r^{(0)} = p_j^{(0)} = 0$, $\psi^{(0)} = \psi_0$ and $f_z^{(0)} = 0$ i.e. the material is at rest and homogeneous and $\psi_0 \in [0, 1[$ is the given initial reduced volume fraction. When $n \geq 1$, let us assume by recurrence that the numerical solution of system (Q) is given at time t_{n-1} , i.e. $\left(u_z^{(n-1)}, w_z^{(n-1)}, w_r^{(n-1)}, \psi^{(n-1)}, f_z^{(n-1)}, p_j^{(n-1)}\right)$ is known. Then, $\left(u_z^{(n)}, w_z^{(n)}, w_r^{(n)}, \psi^{(n)}, f_z^{(n)}, p_j^{(n)}\right)$ is computed using the following fixed point procedure.

Let $k \in \mathbb{N}$ denotes the index of the fixed point inner loop. At each step $n \geq 1$, a sequence $\left(u_z^{(n,k)}, w_z^{(n,k)}, w_r^{(n,k)}, \psi^{(n,k)}, f_z^{(n,k)}, p_j^{(n,k)}\right)_{k \geq 0}$ is defined by recurrence. When $k = 0$, this inner loop is initialised from the values at the previous time step, i.e.

$$\begin{aligned} &\left(u_z^{(n,0)}, w_z^{(n,0)}, w_r^{(n,0)}, \psi^{(n,0)}, f_z^{(n,0)}, p_j^{(n,0)}\right) = \\ &\left(u_z^{(n-1)}, w_z^{(n-1)}, w_r^{(n-1)}, \psi^{(n-1)}, f_z^{(n-1)}, p_j^{(n-1)}\right). \end{aligned}$$

When $k \geq 1$, let us assume by recurrence that $\left(u_z^{(n,k-1)}, w_z^{(n,k-1)}, w_r^{(n,k-1)}, \psi^{(n,k-1)}, f_z^{(n,k-1)}, p_j^{(n,k-1)}\right)$ is known. Then, $\left(u_z^{(n,k)}, w_z^{(n,k)}, w_r^{(n,k)}, \psi^{(n,k)}, f_z^{(n,k)}, p_j^{(n,k)}\right)$ is defined by splitting (Q) into three subsystems, two of them are linear and will be referred as (S1) and (S2), the third one is a congested nonlinear problem, referred as (S3).

By introducing two numerical parameters, k_{max} and ε_{fp} , a stopping criterion is defined:

$$\begin{aligned} &\|\psi^{(n,k-1)} - \psi^{(n,k)}\|^2 + \|w_r^{(n,k-1)} - w_r^{(n,k)}\|^2 \\ &+ \|w_z^{(n,k-1)} - w_z^{(n,k)}\|^2 + \|u_z^{(n,k-1)} - u_z^{(n,k)}\|^2 \leq \sqrt{2} \Delta t \varepsilon_{fp} \quad \text{or } k > k_{max} \end{aligned} \quad (5)$$

where $\|\cdot\|$ denotes the usual L^2 norm with axisymmetric weighting, defined for all function f by

$$\|f\| = \left(\int_0^1 f(r) r \, dr \right)^{\frac{1}{2}}$$

When stopping criterion (5) is satisfied, the fixed point loop is terminated and the last element of the sequence is simply denoted as $\left(u_z^{(n)}, w_z^{(n)}, w_r^{(n)}, \psi^{(n)}, f_z^{(n)}, p_j^{(n)}\right)$, i.e. the second index k is omitted.

With the notations defined above, the two linear subsystems solved at each fixed point iteration write:

(S₁): find $u_z^{(n,k)}$ defined in $]0, 1[$ and $f_z^{(n,k)} \in \mathbb{R}$ such that

$$\left\{ \begin{array}{l} \frac{Re}{\Delta t} \left(u_z^{(n,k)} - u_z^{(n-1)} \right) \\ - \frac{\partial_r}{r} \left(r \eta_{app} \left(\psi^{(n,k-1)} \right) \partial_r u_z^{(n,k)} \right) + f_z^{(n,k)} = 0 \text{ in }]0, 1[\end{array} \right. \quad (6a)$$

$$\int_0^1 u_z^{(n,k)} r \, dr = \frac{1}{4} \quad (6b)$$

$$\partial_r u_z^{(n,k)}(r=0) = u_z^{(n,k)}(r=1) = 0 \quad (6c)$$

(S₂): find $w_z^{(k,n)}$ defined in $]0, 1[$ such that

$$\left\{ \begin{array}{l} \frac{Re \phi_m \psi^{(n,k-1)}}{\Delta t} \left(w_z^{(n,k)} - w_z^{(n-1)} \right) + \varepsilon^{-2} s \left(\psi^{(n,k-1)} \right) w_z^{(n,k)} \\ - \frac{\partial_r}{r} \left(r s \left(\psi^{(n,k-1)} \right) \partial_r w_z^{(n,k)} \right) \\ = \frac{Re \phi_m \psi^{(n,k-1)}}{\Delta t} \left(u_z^{(n,k)} - u_z^{(n-1)} \right) \text{ in }]0, 1[\end{array} \right. \quad (7a)$$

$$\partial_r w_z^{(n,k)}(r=0) = w_z^{(n,k)}(r=1) = 0 \quad (7b)$$

Similarly, the nonlinear congested subsystem write:

(S₃): find $w_r^{(n,k)}$, $p_j^{(n,k)}$ and $\psi^{(n,k)}$ defined in $]0, 1[$ such that

$$\left\{ \begin{array}{l} \frac{Re \phi_m \psi^{(n,k-1)}}{\Delta t} \left(w_r^{(n,k)} - w_r^{(n-1)} \right) + \varepsilon^{-2} s \left(\psi^{(n,k-1)} \right) w_r^{(n,k)} \\ - \frac{\partial_r}{r} \left(2 r s \left(\psi^{(n,k-1)} \right) \partial_r w_r^{(n,k)} \right) + \partial_r p_j^{(n,k)} \\ = \frac{\partial_r}{r} \left(r \eta_{n,r} \left(\psi^{(n,k-1)} \right) \left| \partial_r u_z^{(n,k)} \right| \right) \end{array} \right. \text{ in }]0, 1[\quad (8a)$$

$$\begin{aligned} & - \frac{1}{r} \eta_{n,\theta} \left(\psi^{(n,k-1)} \right) \left| \partial_r u_z^{(n,k)} \right| \\ & 0 \leq \left(\psi^* - \psi^{(n,k)} \right) \perp p_j^{(n,k)} \geq 0 \text{ in }]0, 1[\end{aligned} \quad (8b)$$

$$\frac{1}{\Delta t} \left(\psi^{(n,k)} - \psi^{(n-1)} \circ X^{(n,k-1)} \right) + \frac{\partial_r}{r} \left(r w_r^{(n,k)} \right) \psi^{(n,k)} = 0 \text{ in }]0, 1[\quad (8c)$$

$$w_r^{(n,k)}(r=0) = w_r^{(n,k)}(r=1) = 0 \quad (8d)$$

where $X^{(n,k-1)}(r) = r - \Delta t w_r^{(n,k-1)}(r)$ in (8c) denotes a first order approximation of the characteristics.

Observe that the original unilateral constraint $\psi \leq 1$ has been replaced in (8b) by $\psi^{(n,k)} \leq \psi^*$, where $\psi^* < 1$ is a numerical threshold close to 1. This threshold is used to ensure that the hindrance function s and the viscosities η_{app} , $\eta_{n,r}$ and $\eta_{n,\theta}$ remain bounded. This strategy constitutes an effective regularisation of the constitutive law in order to avoid divergence of the stress components and drag force in the saturated regions.

The two linear systems (S_1) and (S_2) are standard, while the solution of the congested nonlinear system (S_3) requires more work. Observe that (8c) can be explicitly solved in term of $\psi^{(n,k)}$ as:

$$\left(1 + \Delta t \frac{\partial_r}{r} \left(r w_r^{(n,k)}\right)\right) \psi^{(n,k)} = \psi^{(n-1)} \circ X^{(n,k-1)} \quad (9)$$

Indeed, for sufficiently small $\Delta t > 0$, the first factor of the left-hand side of (8c) is strictly positive in $]0, 1[$, and thus $\psi^{(n,k)}$ is well-defined by an explicit expression. This expression of $\psi^{(n,k)}$ can then be replaced in (8b). After rearrangements, we obtain a constraint in terms of $w_r^{(n,k)}$:

$$-\frac{1}{\Delta t} \left(\psi^* - \psi^{(n,k-1)} \circ X^{(n,k-1)}\right) \leq \frac{\partial_r}{r} \left(r w_r^{(n,k)}\right) \perp p_j^{(n,k)} \geq 0$$

This complementarity condition means that the compressibility of the particle phase is bounded negatively, depending on the value of the volume fraction.

Hence, congested subsystem interprets as an obstacle problem coupled to an advection equation :

(\tilde{S}_3): find $w_r^{(n,k)}$ and $p_j^{(n,k)}$, defined in $]0, 1[$, such that

$$\left\{ \begin{array}{l} \frac{Re \phi_m \psi^{(n,k-1)}}{\Delta t} \left(w_r^{(n,k)} - w_r^{(n-1)}\right) + \varepsilon^{-2} s \left(\psi^{(n,k-1)}\right) w_r^{(n,k)} \\ \quad - \frac{\partial_r}{r} \left(2 r s \left(\psi^{(n,k-1)}\right) \partial_r w_r^{(n,k)}\right) + \partial_r p_j^{(n,k)} \\ \quad = \frac{\partial_r}{r} \left(r \eta_{n,r} \left(\psi^{(n,k-1)}\right) \left|\partial_r u_z^{(n,k)}\right|\right) \\ \quad \quad \quad - \frac{1}{r} \eta_{n,\theta} \left(\psi^{(n,k-1)}\right) \left|\partial_r u_z^{(n,k)}\right| \\ -\frac{1}{\Delta t} \left(\psi^* - \psi^{(n,k-1)} \circ X^{(n,k-1)}\right) \leq \frac{\partial_r}{r} \left(r w_r^{(n,k)}\right) \perp p_j^{(n,k)} \geq 0 \text{ in }]0, 1[\quad (10b) \\ w_r^{(n,k)}(r=0) = w_r^{(n,k)}(r=1) = 0 \quad (10c) \end{array} \right. \quad \text{in }]0, 1[\quad (10a)$$

As soon as $w_r^{(n,k)}$ is known, $\psi^{(n,k)}$ can be explicitly computed from (9).

We recognise in (\tilde{S}_3) the standard *obstacle problem* in mathematical physics (see e.g. [50, 51, 52]). It is expressed here in term of $w_r^{(n,k)}$ with a convex constraint (10b) on all the interior of the domain $]0, 1[$, where $p_j^{(n,k)}$ is the associated Lagrange multiplier.

3.2. Resolution of the non smooth obstacle sub-problem

Problem (\tilde{S}_3) defined above can be solved efficiently, without any regularisation, by an augmented Lagrangian method described in this subsection. Since there is no ambiguity, indices n and k are omitted here on the unknowns. The problem

becomes:

(O): find w_r and p_j , defined in $]0, 1[$, such that

$$\begin{cases} \kappa w_r - \frac{\partial_r}{r} (r \beta \partial_r w_r) + \partial_r p_j = f \text{ in }]0, 1[& (11a) \\ g \leq \frac{\partial_r}{r} (r w_r) \perp p_j \geq 0 \text{ in }]0, 1[& (11b) \\ w_r(r=0) = w_r(r=1) = 0 & (11c) \end{cases}$$

where the following notations are introduced for the known data:

$$\begin{aligned} \kappa &= Re \phi_m \psi^{(n,k-1)} \\ \beta &= 2s \left(\psi^{(n,k-1)} \right) \\ f &= \kappa w_r^{(n-1)} + \frac{\partial_r}{r} \left(r \eta_{n,r} \left(\psi^{(n,k-1)} \right) \left| \partial_r u_z^{(n,k)} \right| \right) - \frac{1}{r} \eta_{n,\theta} \left(\psi^{(n,k-1)} \right) \left| \partial_r u_z^{(n,k)} \right| \\ g &= -\frac{1}{\Delta t} \left(\psi^* - \psi^{(n,k-1)} \circ X^{(n,k-1)} \right) \end{aligned}$$

Let L^2 , H^1 , H^{-1} , and H_0^1 denote the usual Hilbert functional spaces associated with the weight r for the cylindrical coordinates. Let us introduce the following convex subset of L^2 :

$$K = \{ \xi \in L^2 ; \xi \geq g \}$$

Note that K is indeed convex, since each convex combinations of any elements of K belongs to K . Let us also introduce the following bilinear and linear forms, defined for all $w, v \in H^1$ and $q \in L^2$ by:

$$\begin{aligned} a(w, v) &= \int_0^1 (\kappa w v + \beta \partial_r w \partial_r v) r dr \\ b(w, q) &= \int_0^1 \partial_r (r w) q dr \\ \ell(v) &= \int_0^1 f v r dr \end{aligned}$$

With $\kappa, \beta \in L^\infty$, and $f \in H^{-1}$, where L^∞ denotes the space of bounded functions. Hence, these forms are well-defined.

Moreover, we assume that $g \in L^2$. Let B denotes the linear operator from H^1 to L^2 associated to the bilinear form b and defined for all $v \in H^1$ by

$$Bv = r^{-1} \partial_r (r v).$$

It interprets as the divergence operator in the axisymmetric tube section. The quadratic function J is defined for all $v \in H^1$ by

$$J(v) = \frac{1}{2} a(v, v) - \ell(v)$$

Problem (O) then expresses as a convex minimisation problem:

$$\begin{aligned} w_r &= \arg \min_{v \in H_0^1} J(v) \\ &\text{subject to } Bv \in K \end{aligned}$$

Note that the convex set K is not a vector space. Thus, the previous optimisation problem is difficult to solve by finite element method, which is based on vector space approximations of functional spaces. For this reason, we introduce the indicator function $\mathbb{I}_K : L^2 \rightarrow [0, \infty]$, defined for all $\xi \in L^2$ by:

$$\mathbb{I}_K(\xi) = \begin{cases} 0 & \text{when } \xi \in K \\ \infty & \text{otherwise} \end{cases}$$

Observe that \mathbb{I}_K is a convex function since K is a convex set. The problem can then be rewritten as:

$$w_r = \arg \min_{v \in H_0^1} J(v) + \mathbb{I}_K(Bv)$$

The problem now expresses as an unconstrained minimisation problem of a convex non-differentiable function on a vector space, which is more suitable to a finite element approximation. The main difficulty is to minimise with respect to $\mathbb{I}_K(Bv)$, which is the non-differentiable part. A solution is to introduce an auxiliary variable δ , together with the additional constraint $\delta = Bw$ and its associated Lagrange multiplier, which shall coincide with the jamming pressure p_j . We then introduce the following augmented Lagrangian (see e.g. [53]):

$$L(v, \xi ; q) = J(v) + \mathbb{I}_K(\xi) + \int_0^1 (\xi - Bv) q r dr + \frac{\mu}{2} \int_0^1 (\xi - Bv)^2 r dr \quad (12)$$

where $\mu > 0$ is the augmentation parameter. The problem is equivalent to finding the following saddle point:

$$(w_r, \delta ; p_j) = \arg \min_{\substack{v \in H_0^1 \\ \xi \in L^2}} \max_{q \in L^2} L(v, \xi ; q)$$

Observe that the term factored by the augmentation parameter μ in (12) is the square of the constraint: the saddle-point of the Lagrangian L is thus independent of μ . The numerical parameter μ only influences the convergence of minimisation algorithm.

The solution is computed by an Uzawa descent method, fully described in [Appendix C](#).

3.3. Finite element spatial discretisation

The dimensionless space interval $[0, 1]$ is discretised by a uniform mesh whose step is denoted $h > 0$. Components u_z , w_z and w_r of the velocities are approximated by continuous and piecewise quadratic functions, while the reduced

volume fraction ψ , the jamming pressure p_j and the divergence δ are approximated by continuous and piecewise linear functions. The algorithm described in the previous subsections is implemented using Rheolef C++ finite element library [54]. Four different values of dimensionless mesh size h were investigated, namely $h = 1/200, 1/400, 1/800, \text{ and } 1/1600$. The dimensionless time step Δt is adapted according to the value of h as follows: $\Delta t = 400h$. Hence, for each refinement of the mesh, the time step is divided by two.

Final computation time T is set such that steady-state flow regime is reached. In practice, the time needed to reach this steady state depends on the value of average volume fraction ϕ_0 . For most of the numerical tests presented below (subsections 4.2, 4.3, 4.4), an arbitrary large value $T = 4000$ was chosen. When comparing results obtained for different values of ϕ_0 (subsections 4.4 and 4.5), the value of T was adapted according to a proper steady-state criterion, as explained later.

4. Results and discussion

This section is dedicated to a preliminary exploration of the predictions of the new migration model presented in this paper. The solutions, computed with the algorithm presented in the previous section, are compared with experimental results obtained by Oh et al. [18]. This section starts with a presentation of the experimental setup and the choice of model material parameters. Then, validations of our numerical algorithm are presented. We start by a study of the convergence of the residual terms in the two inner loops of the implicit time discretisation scheme, and then turn to the convergence of the solution versus mesh refinement. Finally, the main physical features of the solution are described, together with preliminary comparisons to experimental data and a sensitivity analysis with respect to maximum volume fraction ϕ_m .

4.1. Experimental setup

symbol	value	unit
ρ	1056	kg.m ⁻³
η_0	3.6	Pa.s
r_p	7×10^{-5}	m
R	3.15×10^{-3}	m
q	3.14×10^{-8}	m ³ .s ⁻¹
ϕ_0	0.32 ; 0.5	
ϕ_m	0.585 – 0.64	

symbol	value	unit
K_s	0.6	
K_n	1	
λ_2	0.9	
λ_3	0.5	
α	3	

Table 2: Values of model material parameters.

Oh et al. [18] injected a mono-disperse particle suspension in a circular tube from a tank with an imposed flow rate q . At the inlet of the tube, the volume

fraction is supposed to be uniform, equal to ϕ_0 . Particle volume fraction ϕ and axial velocity of the mixture u_z were measured by MRI at a sufficiently long distance from the inlet to ensure fully developed flow. Note that this distance, at which the flow can be considered as fully developed, depends upon several parameters [18]: the volume fraction at the inlet of the tube ϕ_0 , the density of both the fluid and the particles, the fluid viscosity η_0 , the particle radius r_p , and the tube radius R . Inlet flow rate was varied between 0.5 and 3 ml/min. For the computations presented thereafter, we retained an intermediate value $q = 1.88$ ml/min.

The values of model constants chosen for the computations presented in this section are summarised in Table 2. The parameters K_n , K_s , λ_2 , λ_3 and α of the rheological model were identified from experimental data, as explained in Appendix D. The choice of the maximum volume fraction ϕ_m will be discussed in the forthcoming paragraph dedicated to comparisons with experiments.

4.2. Convergence of the inner loops

This paragraph documents the convergence of the augmented Lagrangian loop and the fixed point loop. These numerical tests were performed with values of $\phi_0 = 0.32$, $\phi_m = 0.585$, and an arbitrary final time $T = 4000$. The link between h and Δt is provided by Table 4. Fig. 2.left plots the relative error in L^2

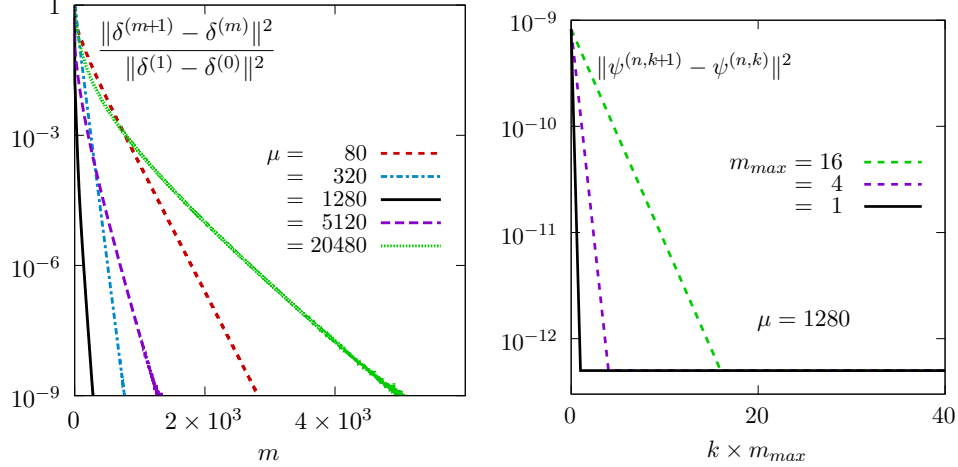


Figure 2: Convergence of the two inner loops at $t = 3T/8$ ($h = 1/800$). (left) Convergence of the augmented Lagrangian loop: normalised relative error on the auxiliary variable $\delta^{(m)}$ versus iteration number m for different values of augmentation parameter μ . (right) Convergence of the fixed point loop: relative error for the volume fraction $\psi^{(n,k)}$ versus total iteration number $k \times m_{max}$ for different values of m_{max} .

norm of the auxiliary variable $\delta^{(m)}$ during the augmented Lagrangian loop as a function of loop index m . The convergence is studied for $k = 0$, i.e. at the first

iteration of the fixed point loop, and for $t = 3T/8$, i.e. fully developed flow is not reached yet. First, observe that the relative error decrease for all values of the augmentation parameter μ , as expected from theory (see Fortin and Glowinski [53]). Next, observe that the convergence is faster for intermediate values of μ : the optimal value is near $\mu = 1280$.

Let us now turn to the convergence of the fixed point loop. Fig. 2.right presents the relative error for the volume fraction $\psi^{(n,k)}$ versus total number of iterations $k \times m_{max}$ of the inner loops. The initial relative error $\|\psi^{(n,1)} - \psi^{(n,0)}\|$ is of about 10^{-9} , and decreases to about 10^{-12} , when rounding effects appear. Hence, the normalised relative error decreases to about 10^{-3} . Recall that there is an inner augmented Lagrangian loop, whose index is m and maximal number of iterations is m_{max} . To understand how the two loops interact, the value of m_{max} has been varied. Observe that it is not necessary to iterate more than once in the augmented Lagrangian loop, for the fixed point loop to converge. Moreover, this strategy appears to be the most efficient in terms of overall convergence rate of the algorithm.

symbol	value	description
μ	1280	augmented Lagrangian parameter
m_{max}	1	inner augmented Lagrangian maximum iteration
k_{max}	40	outer fixed point maximal iteration
ε_{fp}	10^{-12}	fixed point stopping criterion

Table 3: Numerical parameters of the algorithm.

Finally, the numerical parameters retained for the simulations of the next sections are grouped in Table 3. The values of μ , m_{max} and k_{max} ensure proper convergence of the inner loops. The stopping criterion (5) of the fixed point outer loop is set at $\varepsilon_{fp} = 10^{-12}$.

4.3. Spatial and temporal convergences

This paragraph is dedicated to the convergence of the solution versus the simultaneous refinement of the time and space steps. The four considered mesh configurations are summarised in Table 4. Similar to time step Δt that tends to zero with mesh size h , we also considered that the regularisation parameter of the constitutive law ψ^* (effective maximum volume fraction) evolves with mesh refinement, and tends to 1 when $h \rightarrow 0$. Specifically, the following relation was considered based on a specific convergence study (not shown here): $\psi^* = 1 - 10.24h$ (Tab. 4).

As in the previous subsection, these numerical tests were performed for values of $\phi_0 = 0.32$, $\phi_m = 0.585$, and $T = 4000$. In Fig. 3, an additional subscript h is added to variables, e.g. $w_{r,h}$, ψ_h , in order to indicate the mesh dependence. Fig. 3.left plots the L^2 norm of the radial migration velocity $w_{r,h}$ versus dimensionless time t for the four mesh refinements. Observe first that, on all meshes,

$1/h$	Δt	$1 - \psi^*$
200	2	5.12×10^{-2}
400	1	2.56×10^{-2}
800	0.5	1.28×10^{-2}
1600	0.25	0.64×10^{-2}

Table 4: Parameters of the numerical discretisation for dimensionless final time $T = 4000$.

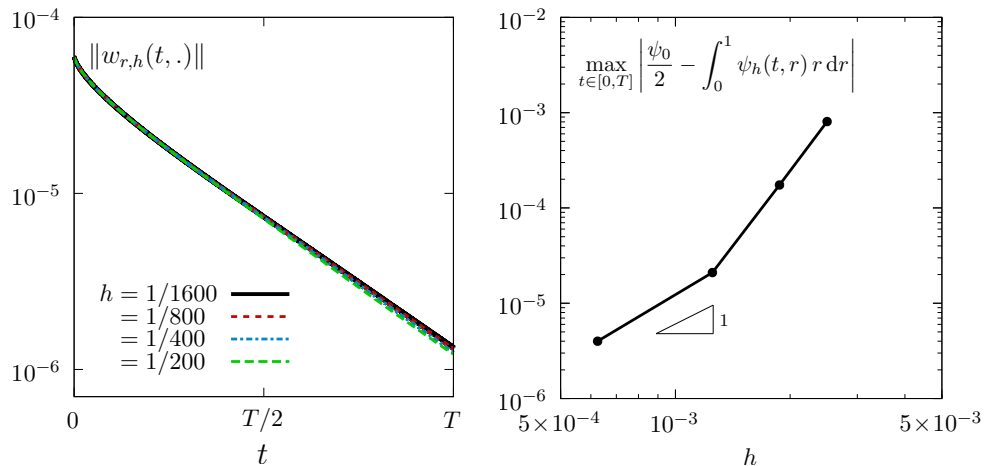


Figure 3: Convergence versus simultaneous space and time refinement (see Table 4), with $T = 4000$, $\phi_0 = 0.32$, $\phi_m = 0.585$. (left) L^2 norm of the radial component $w_{r,h}$ of migration velocity versus dimensionless time t . (right) Maximum particle mass error versus mesh size h .

$w_{r,h}$ decays exponentially with time: as expected, radial particle migration vanishes in steady-state regime. Furthermore, the slope of this decay appears to be mesh-independent.

An important feature of our model is that it should conserve the mass of the fluid and solid phases, as expressed by Eq. (2c) for the whole mixture and Eq. (2d) for the particle phase. At $t = 0$, the particle mass is given by $\int_0^1 \phi_0 r dr = \phi_0/2$. Fig. 3.right shows the maximum particle mass error as a function of mesh size h . Obviously, this error is never exactly zero, as the finite element method only provides an approximation of the solution. However, the error clearly tends to zero and Fig. 3.right suggests that it converges as $\mathcal{O}(h)$, i.e. linearly, with mesh refinement. This linear convergence represents a major improvement compared to other existing migration models. As our formulation enables us to impose a non-penetration boundary condition (2g) on the particle velocity $\mathbf{u} + \mathbf{w}$, or equivalently on \mathbf{w} , it prevents uncontrolled mass loss. Let us recall that this property is made possible by introducing the second-order differential term on \mathbf{w} in (2b).

Fig. 4 presents the radial profiles of various quantities at time $t = T$ for the four mesh refinements. A clear, progressive convergence of all the profiles with h can be observed. Note that the amplitude of radial migration velocity w_r is very small, confirming that the system has reached quasi-steady state. Accordingly, the bulk shear stress $\sigma_{m,rz}$ is observed to evolve linearly within the tube, as expected, for all mesh refinements. The peak of jamming pressure p_j on the symmetry axis $r = 0$ is likely due to a numerical artefact in the treatment of the boundary condition, but appears to remain bounded as $h \rightarrow 0$.

For each mesh size h , one can define a critical radius, denoted as $r_{c,h}(t)$, such that $\psi_h(t, r)$ reaches its maximum $1 - \psi^*$ for all $r \in [0, r_{c,h}(t)]$ (see Fig. 4.top-right). This region corresponds to a central plug, where the radial migration velocity w_r vanishes while the axial bulk velocity u_z is constant and maximum. Table 5 indicates the values of $r_{c,h}$ at time $t = T$ for the four mesh refinements (see also Tab. 4). The last column corresponds to the difference with the value obtained for the finest subdivision. Observe that this difference decreases regularly when $h \rightarrow 0$, and suggests that the critical radius converges as $\mathcal{O}(h)$.

h	$r_{c,h}(T)$	$ r_{c,h} - r_{c,h_4} $
1/200	0.240	0.033
1/400	0.222	0.015
1/800	0.214	0.007
1/1600	0.207	

Table 5: Convergence of critical plug radius $r_{c,h}$ versus mesh refinement h .

4.4. Main features of the solution

This subsection describes the main features of the solution predicted by the present migration model. The finest mesh, namely $h = 1/1600$, is retained for these computations.

Fig. 5 shows the radial profiles of various physical quantities in the tube section at three different times. Note that values of $\phi_0 = 0.32$, $\phi_m = 0.585$, and $T = 4000$ are still used here. It is observed that the central plug, in which the material is saturated ($\psi = \psi^*$), grows over time. At the transition between the plug and the outer sheared region ($r = r_c(t)$), the reduced volume fraction ψ is continuous but not differentiable. As already mentioned, the radial migration velocity w_r strongly decreases with time, and vanishes in the plug. Negative values of w_r in the sheared region indicate that particles migrate from the wall to the centre of the tube, as expected. Interestingly, one also observes that the values of longitudinal migration velocity w_z remain slightly negative even at steady-state, indicating that particle velocity lags behind fluid velocity. As expected from the complementarity condition (11b), the jamming pressure p_j is nonzero inside this plug, while it is zero in the unsaturated sheared zone. Jamming pressure p_j appears to increase towards the centre of the plug, as do the components of

the particle stress tensor $\boldsymbol{\tau}_{p,rz}$ and $(\boldsymbol{\tau}_p)$. Note however that stress values in the plug are likely to be strongly influenced by the considered regularisation for the constitutive law. One cannot argue that stress profiles in this region converge to those that would be obtained with a more sophisticated constitutive law avoiding the need for a regularisation. Finally, also observe that the jamming pressure displays a small discontinuity at the transition between the plug and the sheared region at intermediate times, but that this discontinuity tends to vanish in the steady-state regime.

Steady-state solutions have been computed for five different values of average reduced volume fraction ψ_0 ranging between 0.55 and 0.78. The corresponding values of ϕ_0 and ϕ_m are indicated in Figure 6. The final computation time T used for each case was varied to ensure that a fully-developed flow regime is effectively reached. For that purpose, a steady-state criterion based on the exponential decay of w_r (see Fig. 3.left) is used. More precisely, the time loop is stopped when $\|w_r(t)\|$ is reduced by a factor of 100 compared to its value at the end of the first iteration. Observe that the final dimensionless time T decreases as the average reduced volume fraction ψ_0 increases (see Fig. 6).

Figure 7 illustrates the influence of average volume fraction ϕ_0 on the steady-state solution, for a fixed value of ϕ_m . As expected, the width of the plug region strongly increases with ϕ_0 , while the average bulk velocity decreases. The jamming pressure in the plug, as well as the different components of the particle stress tensor, are also observed to increase when ϕ_0 increases. For completeness, let us also mention that the Lagrange multiplier f_z is negative and decreases with ϕ_0 : steady-state values are $f_z(T) = -10.80$ for $\phi_0 = 0.32$ and $f_z(T) = -43.84$ for $\phi_0 = 0.50$. Recall that f_z interprets as the longitudinal gradient of the bulk pressure.

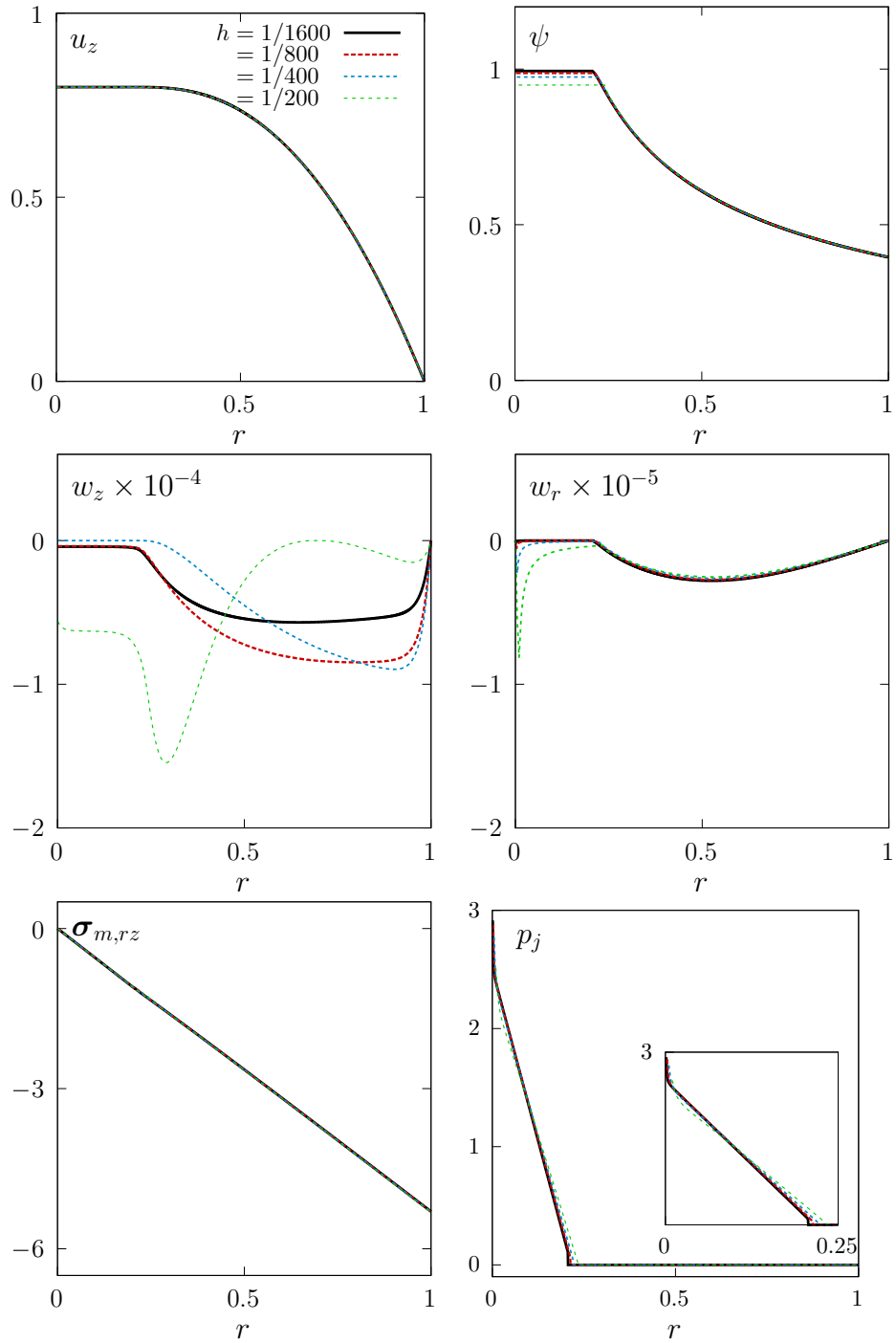


Figure 4: Convergence versus mesh refinement: radial profiles at $t = T = 4000$ of longitudinal bulk velocity u_z , reduced particle volume fraction ψ , radial and longitudinal migration velocity w_r and w_z , bulk shear stress $\sigma_{m,rz}$, and jamming pressure p_j ($\phi_0 = 0.32$, $\phi_m = 0.585$).

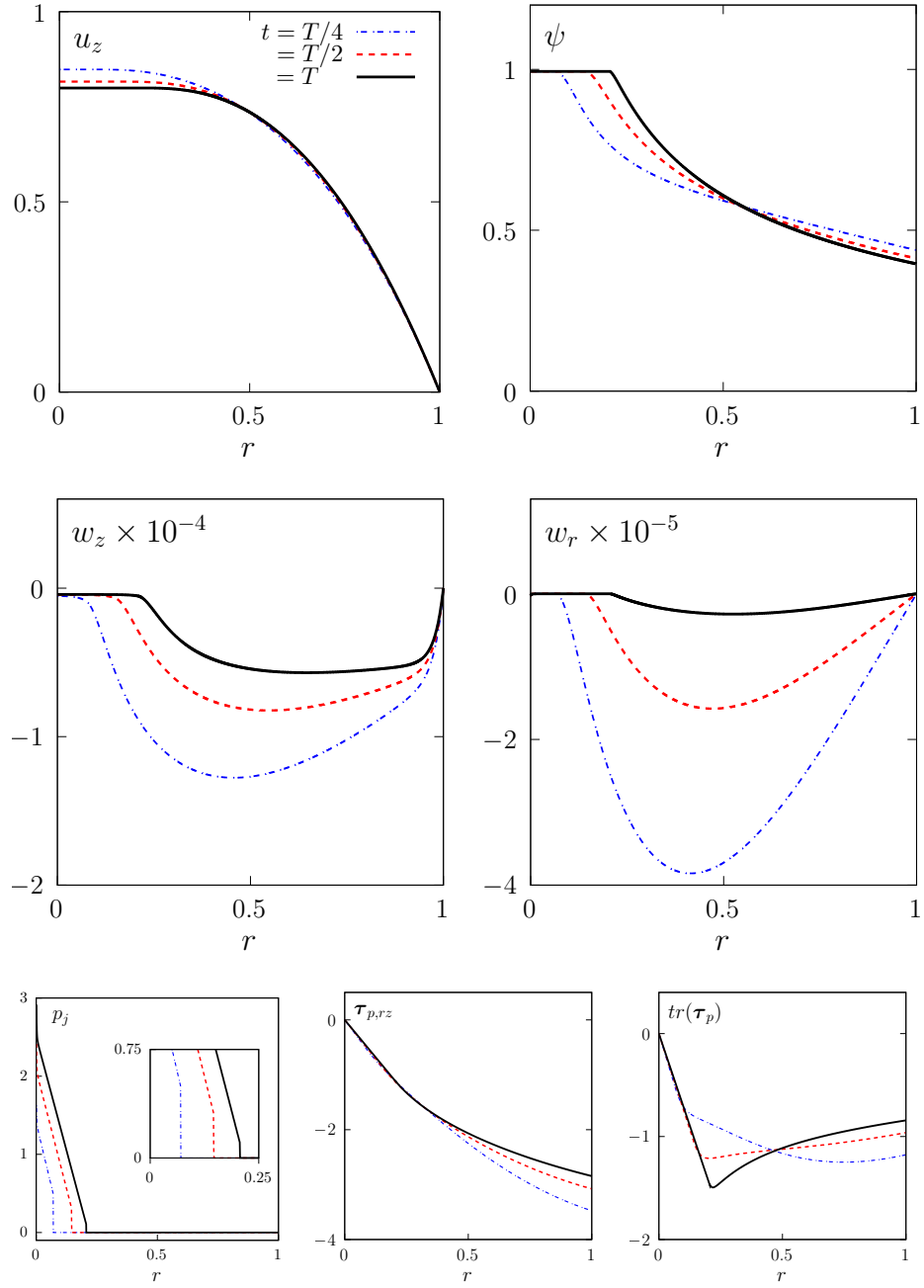
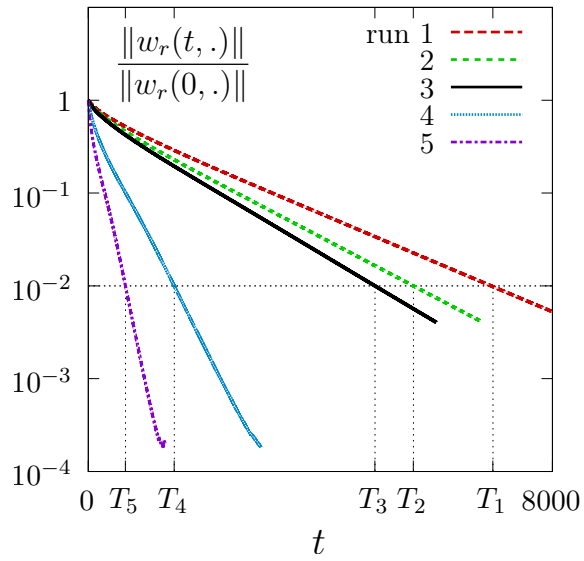


Figure 5: Convergence of the solution to the steady state: radial profiles at three different times of longitudinal bulk velocity u_z , reduced particle volume fraction ψ , radial and longitudinal migration velocity w_r and w_z , jamming pressure p_j , and particle stress shear and spherical component $\tau_{p,rz}$ and $\text{tr}(\tau_p)$. Final dimensionless time is $T = 4000$ ($\phi_0 = 0.32$, $\phi_m = 0.585$, $h = 1/1600$).



run	1	2	3	4	5
ϕ_0	0.32			0.50	
ϕ_m	0.585	0.60	0.64	0.585	0.64
ψ_0	0.55	0.53	0.50	0.85	0.78
T	6973	5603	4940	1481	640

Figure 6: Final dimensionless computation time T , for which $|w_r|$ is reduced by a factor of 100 with respect to its initial value, for the five simulation runs discussed in the text. The corresponding values of average reduced volume fraction $\psi_0 = \phi_0/\phi_m$, average volume fraction ϕ_0 , and maximal volume fraction ϕ_m , are indicated in the table. Other parameters are given in Table 2. Finest mesh size $h = 1/1600$ is used.

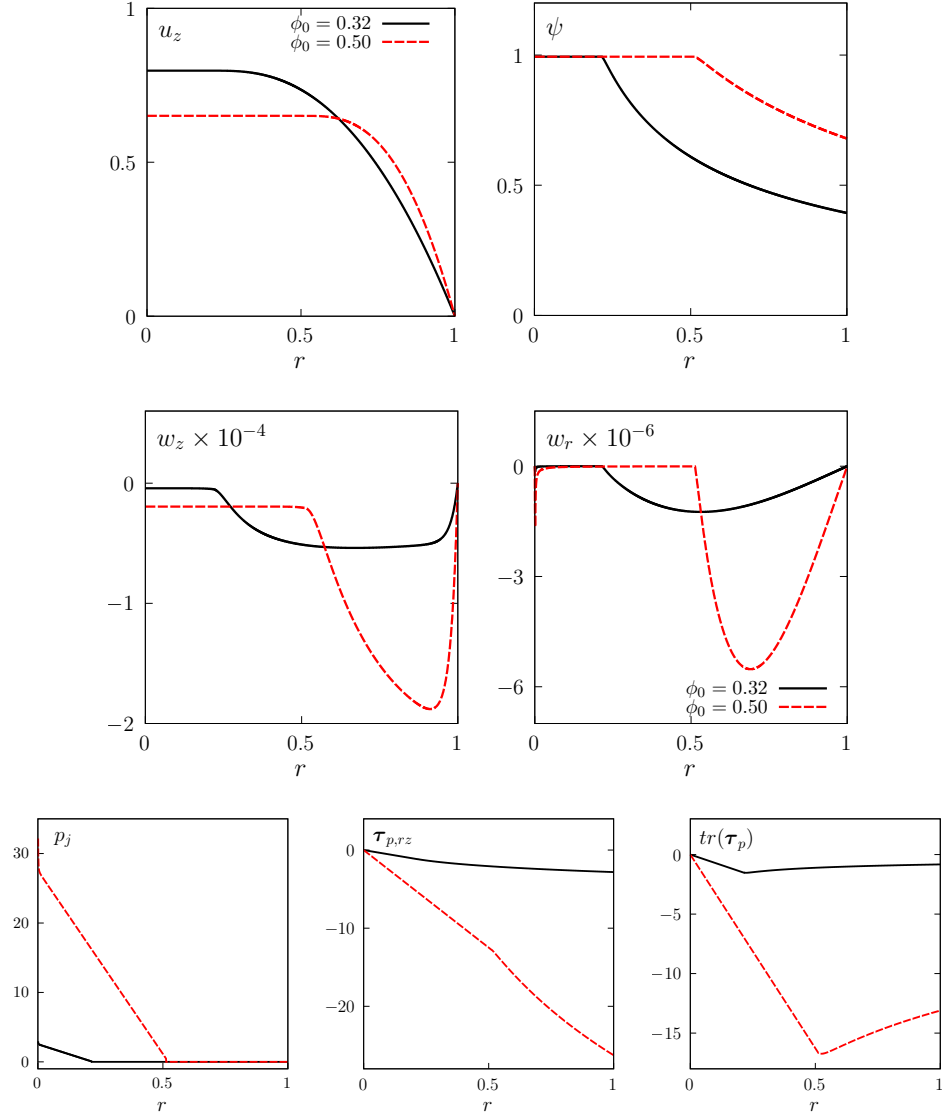


Figure 7: Comparison of the steady-state solutions for two different values of initial volume fraction $\phi_0 = 0.32$ and 0.50 , while $\phi_m = 0.585$ ($h = 1/1600$). Radial profiles of longitudinal bulk velocity u_z , reduced particle volume fraction ψ , radial and longitudinal migration velocity w_r and w_z , jamming pressure p_j , and particle stress shear and spherical component $\tau_{p,rz}$ and $\text{tr}(\tau_p)$.

4.5. Comparison with experiments

This paragraph presents direct comparisons between the experimental measurements of Oh et al. [18], performed on fully developed flows, and steady-state solutions of our migration model. Oh et al. [18] report data for several values of average particle volume fraction ϕ_0 . We retained here the results corresponding to a semi-concentrated and to a concentrated case, with nominal values $\phi_0 = 0.35$ and $\phi_0 = 0.52$ respectively. We observed that these nominal values of volume fraction slightly differ from the values obtained by direct integration of the measured radial particle fraction profiles. This computation leads to effective values $\phi_0 = 0.32$ and $\phi_0 = 0.5$ for the semi-concentrated and concentrated cases, respectively. To avoid systematic discrepancies between experimental and numerical profiles, the model solutions were computed for these effective values of ϕ_0 .

Choosing the value of the maximal volume fraction ϕ_m in the model requires care. As explained by Lecampion and Garagash [15], volume fraction ϕ is actually characterised by two noticeable limits in highly-concentrated mixtures. The first limit is the random close packing fraction $\phi_{rcp} = 0.64$, which cannot be exceeded. The second limit is the critical volume fraction $\phi_c \approx 0.585$, above which the mixture is jammed, i.e. behaves as a solid. In regions where $\phi > \phi_c$, volume fraction can still continue to increase by compaction, as the particle phase behaves as a compressible solid. As shown by Oh et al. [18], the actual steady-state volume fraction reached in the jammed regions depends upon ϕ_0 . We may hypothesise that this steady-state volume fraction results from a complex balance between particle jamming pressure p_j and friction. Since the constitutive law of Morris and Boulay [7] considered in the present model does not account for friction nor for solid compressibility in the jammed regions, the apparent maximal volume fraction ϕ_m to be considered remains a priori unknown in the range $[\phi_c, \phi_{rcp}]$. Accordingly, for each average volume fraction ϕ_0 , solutions corresponding to several values of maximal volume fraction ϕ_m were computed and compared to experimental data.

Fig. 8 presents comparisons between the steady-state solution at $t = T$ and experimental measurements for the semi-concentrated case ($\phi_0 = 0.32$). It is observed that the radial profile of mixture velocity u_z across the tube section is very well reproduced by the model, and this for all choices of ϕ_m in the range 0.585–0.64 (see Fig. 8.top-left). In particular, the velocity value in the plug appears to be well captured. Concerning particle volume fraction ϕ (see Fig. 8.top-right), discrepancies can be observed concerning the width of the plug and the sharpness of the transition with the sheared layer. Experimental data seem to indicate thinner plugs, and a smoother transition between the two zones. Note however that the evolution of ϕ in the vicinity of the wall of the tube is well reproduced by the model. It is also observed that, while the choice of ϕ_m in the model has obviously a direct impact on the value of particle volume fraction reached in the plug, this parameter has only little influence on the profiles of ϕ in the sheared region. Experimental measurements appear to

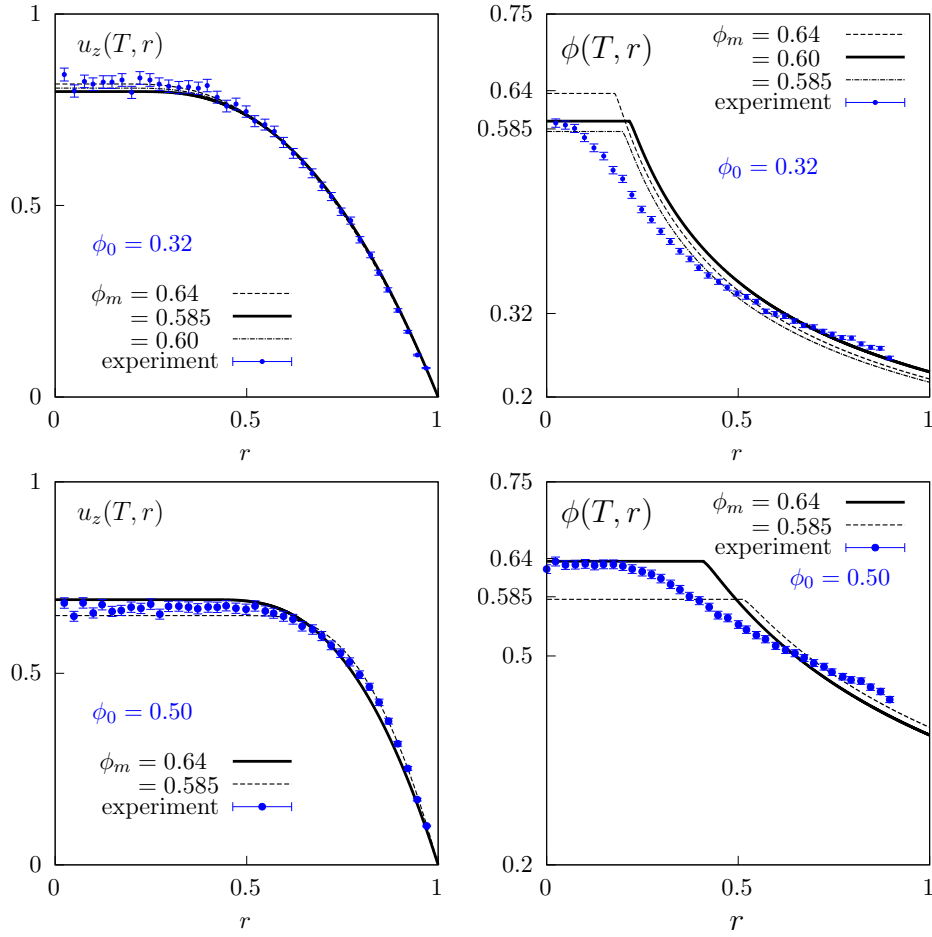


Figure 8: Comparisons of the present migration model with experimental results of Oh et al. [18] for the fully developed flow regime: steady-state radial profiles of bulk longitudinal velocity u_z and particle volume fraction ϕ . (top) Semi-concentrated case $\phi_0 = 0.32$. (bottom) Concentrated case $\phi_0 = 0.50$. Error bars on the experimental data correspond to uncertainties estimated by Oh et al. [18], based on measurements for the interstitial fluid and might thus be underestimated for concentrated mixtures.

be best captured with $\phi_m = 0.60$ in this case.

Similar observations can be made for the concentrated case ($\phi_0 = 0.50$). Here also, the radial profile of u_z is well reproduced in the whole tube section for all choices of ϕ_m (see Fig. 8.bottom-left). In this case, the value of volume fraction in the central plug is best captured with the upper bound $\phi_m = 0.64$ (see Fig. 8.bottom-right), suggesting that the maximum volume fraction reached in the plug appears to increase with the average concentration of the suspension. In contrast, it is again observed that the value of ϕ near the wall depends only slightly on the choice of ϕ_m .

The discrepancies between numerical solutions and experimental measurements observed on volume fraction profiles are probably attributable to the limitation of the model pointed out above, namely that the constitutive law for the particle phase does not account for friction and solid compressibility in jammed regions. Experimental results clearly indicate that volume fraction continues to increase beyond ϕ_c in the plug, and saturates only when reaching the limit $\phi = \phi_{rcp}$. In contrast, in the model, a single maximum value ϕ_m is considered. Extension of the constitutive law to account for such granular processes, as proposed by Lecampion and Garagash [15], thus represents a promising prospect to further improve the agreement with experimental data.

5. Conclusion and perspectives

This paper presents a new migration model for mono-disperse suspensions of neutrally buoyant particles. Unlike suspension balance model (SBM), which relies on a single velocity formulation [25], our model involves two velocities and two pressures. The two-velocity formulation, coupled to the introduction of a diffusive term on the migration velocity \mathbf{w} , allows us to properly impose non-penetration boundary conditions for the particles across walls, and thus to satisfy rigorous mass conservation for the particle phase. Physically, the new diffusive term can be interpreted as a non-local contribution to the particle stresses in unjammed regions. In addition, the unilateral constraint $\phi \leq \phi_m$ on the particle volume fraction is strictly imposed through the introduction of a particle jamming pressure p_j . This Lagrange multiplier, which takes nonzero values only in jammed regions, interprets as the contribution to the particle pressure of the collective interactions (contact chains) that develop between particles in these regions.

Through an asymptotic analysis, a reduced 1D migration model is derived in the case of an axisymmetric Poiseuille flow, and a fully implicit algorithm is proposed for computing numerical solutions of this reduced model. The originality lies in the handling of the unilateral constraint, through an augmented Lagrangian method embedded in a fixed point iteration at each time step. This algorithm is coupled to a finite element spatial discretisation, and the convergence properties of the scheme are carefully demonstrated. In particular, the inner loops involved in the augmented Lagrangian and the fixed point are shown to converge in a small number of iterations. The error on particle mass is also shown to converge linearly with mesh refinement.

The physical characteristics of the solutions are described as a function of average volume fraction, and quantitative comparisons with experimental measurements in fully-developed flow regime [18] are presented for both a semi-concentrated and a concentrated case. Mixture velocity profiles, characterised by the formation of a central plug, appear to be very well reproduced. The model is thus able to accurately capture the effects of jamming and the effective viscoplastic behavior [1] in highly-concentrated mixtures. Discrepancies between model predictions and experimental data remain nevertheless visible on the volume fraction profiles, particularly at the transition between the plug and the outer sheared region. In experiments, the transition between the two zones appears smoother than in the numerical solutions.

To overcome the current limitations of the model, future improvements shall concentrate on including more sophisticated constitutive relations accounting for specific granular processes in concentrated regions. In particular, inelastic compressibility beyond the jamming limit seems to be a necessary ingredient to better capture the evolution of particle volume fraction observed in plug regions [15]. Inclusion of a true yield stress in jammed zones through, e.g., frictional effects Saramito [see, e.g., 55], would also be necessary to avoid the

use of a regularised apparent viscosity and predict more realistic particle stress values in these regions. Finally, the development of anisotropic micro-structures in both jammed and sheared regions could also be considered through specific tensorial constitutive relations [13]. Once these more realistic constitutive models will be implemented and tested, future work shall also consider the extension of the numerical algorithm in order to efficiently address more complex geometries such as 3D channel flows, flows around obstacles [56, 57], or re-suspension experiments [58]. Finally, another promising line of improvement of the numerical resolution would consist in implementing mesh adaptation along the interface between the plug and the sheared region, as done for Bingham fluids by, e.g., Roquet and Saramito [59].

References

- [1] Boyer F, Guazzelli E, Pouliquen O. Unifying suspension and granular rheology. *Phys Rev Lett* 2011;107(18):188301. doi:[10.1103/PhysRevLett.107.188301](https://doi.org/10.1103/PhysRevLett.107.188301).
- [2] Gallier S, Lemaire E, Peters F, Lobry L. Rheology of sheared suspensions of rough frictional particles. *J Fluid Mech* 2014;757:514–49. doi:[10.1017/jfm.2014.507](https://doi.org/10.1017/jfm.2014.507).
- [3] Guazzelli É, Pouliquen O. Rheology of dense granular suspensions. *J Fluid Mech* 2018;852. doi:[10.1017/jfm.2018.548](https://doi.org/10.1017/jfm.2018.548).
- [4] Denn M, Morris J, Bonn D. Shear thickening in concentrated suspensions of smooth spheres in newtonian suspending fluids. *Soft matter* 2018;14(2):170–84. doi:[10.1039/C7SM00761B](https://doi.org/10.1039/C7SM00761B).
- [5] Mari R, Seto R, Morris JF, Denn MM. Shear thickening, frictionless and frictional rheologies in non-brownian suspensions. *J Rheol* 2014;58(6):1693–724. doi:[10.1122/1.4890747](https://doi.org/10.1122/1.4890747).
- [6] Singh A, Mari R, Denn M, Morris J. A constitutive model for simple shear of dense frictional suspensions. *J Rheol* 2018;62(2):457–68. doi:[10.1122/1.4999237](https://doi.org/10.1122/1.4999237).
- [7] Morris JF, Boulay F. Curvilinear flows of noncolloidal suspensions: the role of normal stresses. *J Rheol* 1999;43(5):1213–37. doi:[10.1122/1.551021](https://doi.org/10.1122/1.551021).
- [8] Dbouk T, Lemaire E, Lobry L, Moukalled F. Shear-induced particle migration: Predictions from experimental evaluation of the particle stress tensor. *J Non Newt Fluid Mech* 2013;198:78–95. doi:[10.1016/j.jnnfm.2013.03.006](https://doi.org/10.1016/j.jnnfm.2013.03.006).
- [9] Phan-Thien N, Fan XJ, Khoo BC. A new constitutive model for monodispersed suspensions of spheres at high concentrations. *Rheol Acta* 1999;38:297–304. doi:[10.1007/s003970050181](https://doi.org/10.1007/s003970050181).

- [10] Stickel JJ, Phillips RJ, Powell RL. A constitutive model for microstructure and total stress in particulate suspensions. *J Rheol* 2006;50(4):379–413. doi:[10.1122/1.2209558](https://doi.org/10.1122/1.2209558).
- [11] Goddard JD. A dissipative anisotropic fluid model for non-colloidal particle dispersions. *J Fluid Mech* 2006;568:1–17. doi:[10.1017/S0022112006002333](https://doi.org/10.1017/S0022112006002333).
- [12] Ozenda O, Saramito P, Chambon G. A new rate-independent tensorial model for suspensions of non-colloidal rigid particles in newtonian fluids. *J Rheol* 2018;62:889–903. doi:[10.1122/1.4995817](https://doi.org/10.1122/1.4995817).
- [13] Ozenda O, Saramito P, Chambon G. Tensorial rheological model for concentrated non-colloidal suspensions: normal-stress differences. *J Fluid Mech* 2020;898:A25. doi:[10.1017/jfm.2020.405](https://doi.org/10.1017/jfm.2020.405).
- [14] Chauchat J, Médale M. A three-dimensional numerical model for incompressible two-phase flow of a granular bed submitted to a laminar shearing flow. *Comp Meth App Mech Eng* 2010;199(9-12):439–49. doi:[10.1016/j.cma.2009.07.007](https://doi.org/10.1016/j.cma.2009.07.007).
- [15] Lecampion B, Garagash DI. Confined flow of suspensions modelled by a frictional rheology. *J Fluid Mech* 2014;759:197–235. doi:[10.1017/jfm.2014.557](https://doi.org/10.1017/jfm.2014.557).
- [16] Leighton D, Acrivos A. The shear-induced migration of particles in concentrated suspensions. *J Fluid Mech* 1987;181:415–39. doi:[10.1017/S0022112087002155](https://doi.org/10.1017/S0022112087002155).
- [17] Lyon MK, Leal LG. An experimental study of the motion of concentrated suspensions in two-dimensional channel flow. Part 1. monodisperse systems. *J Fluid Mech* 1998;363:25–56. doi:[10.1017/S0022112098008817](https://doi.org/10.1017/S0022112098008817).
- [18] Oh S, Song YQ, Garagash DI, Lecampion B, Desroches J. Pressure-driven suspension flow near jamming. *Phys Rev Lett* 2015;114(8):088301. doi:[10.1103/PhysRevLett.114.088301](https://doi.org/10.1103/PhysRevLett.114.088301).
- [19] Wachs A, Hammouti A, Vinay G, Rahmani M. Accuracy of finite volume/staggered grid distributed Lagrange multiplier/fictitious domain simulations of particulate flows. *Comput Fluids* 2015;115:154–72. doi:[10.1016/j.compfluid.2015.04.006](https://doi.org/10.1016/j.compfluid.2015.04.006).
- [20] Phillips RJ, Armstrong RC, Brown RA, Graham AL, Abbott JR. A constitutive equation for concentrated suspensions that accounts for shear-induced particle migration. *Phys Fluids A: Fluid Dyn* 1992;4(1):30–40. doi:[10.1063/1.858498](https://doi.org/10.1063/1.858498).
- [21] Jackson R. Locally averaged equations of motion for a mixture of identical spherical particles and a Newtonian fluid. *Chem Eng Sci* 1997;52(15):2457–69. doi:[10.1016/S0009-2509\(97\)00065-1](https://doi.org/10.1016/S0009-2509(97)00065-1).

- [22] Lhuillier D. Migration of rigid particles in non-Brownian viscous suspensions. *Phys Fluids* 2009;21(2):023302. doi:[10.1063/1.3079672](https://doi.org/10.1063/1.3079672).
- [23] Nott PR, Guazzelli E, Pouliquen O. The suspension balance model revisited. *Phys Fluids* 2011;23(4):043304. doi:[10.1063/1.3570921](https://doi.org/10.1063/1.3570921).
- [24] Nott PR, Brady JF. Pressure-driven flow of suspensions: simulation and theory. *J Fluid Mech* 1994;275:157–99. doi:[10.1017/S0022112094002326](https://doi.org/10.1017/S0022112094002326).
- [25] Miller RM, Morris JF. Normal stress-driven migration and axial development in pressure-driven flow of concentrated suspensions. *J Non Newt Fluid Mech* 2006;135(2):149–65. doi:[10.1016/j.jnmfm.2005.11.009](https://doi.org/10.1016/j.jnmfm.2005.11.009).
- [26] Pouliquen O, Belzons M, Nicolas M. Fluctuating particle motion during shear induced granular compaction. *Phys Rev Lett* 2003;91(1):014301. doi:[10.1103/PhysRevLett.91.014301](https://doi.org/10.1103/PhysRevLett.91.014301).
- [27] Gaume J, Chambon G, Naaim M. Microscopic origin of nonlocal rheology in dense granular materials. *Phys Rev Lett* 2020;125:188001. doi:[10.1103/PhysRevLett.125.188001](https://doi.org/10.1103/PhysRevLett.125.188001).
- [28] Bresch D, Perrin C, Zatorska E. Singular limit of a Navier-Stokes system leading to a free/congested zones two-phase model. *Comptes Rendus Math* 2014;352(9):685–90. doi:[10.1016/j.crma.2014.06.009](https://doi.org/10.1016/j.crma.2014.06.009).
- [29] Bresch D, Renardy M. Development of congestion in compressible flow with singular pressure. *Asymp Anal* 2017;103(1-2):95–101. doi:[10.3233/ASY-171421](https://doi.org/10.3233/ASY-171421).
- [30] Lions PL, Masmoudi N. On a free boundary barotropic model. In: *Annal. I.H.P. Non Lin. Anal.*; vol. 16. 1999, p. 373–410. doi:[10.1016/S0294-1449\(99\)80018-3](https://doi.org/10.1016/S0294-1449(99)80018-3).
- [31] Berthelin F, Degond P, Delitala M, Rascle M. A model for the formation and evolution of traffic jams. *Arch Rat Mech Anal* 2008;187(2):185–220. doi:[10.1007/s00205-007-0061-9](https://doi.org/10.1007/s00205-007-0061-9).
- [32] Berthelin F, Broizat D. A model for the evolution of traffic jams in multi-lane. *Kinet Related Mod* 2012;5(4):697–728. doi:[10.3934/krm.2012.5.697](https://doi.org/10.3934/krm.2012.5.697).
- [33] Degond P, Hua J, Navoret L. Numerical simulations of the euler system with congestion constraint. *J Comput Phy* 2011;230(22):8057–88. doi:[10.1016/j.jcp.2011.07.010](https://doi.org/10.1016/j.jcp.2011.07.010).
- [34] Faure S, Maury B. Crowd motion from the granular standpoint. *Math Mod Meth App Sci* 2015;25(03):463–93. doi:[10.1142/S0218202515400035](https://doi.org/10.1142/S0218202515400035).
- [35] Perrin C, Zatorska E. Free/congested two-phase model from weak solutions to multi-dimensional compressible Navier-Stokes equations. *Commun PDE* 2015;40(8):1558–89. doi:[10.1080/03605302.2015.1014560](https://doi.org/10.1080/03605302.2015.1014560).

- [36] Bresch D, Necasova S, Perrin C. Compression effects in heterogeneous media. *J École Poly Math* 2019;6:433–67. doi:[10.5802/jep.98](https://doi.org/10.5802/jep.98).
- [37] Godlewski E, Parisot M, Sainte-Marie J, Wahl F. Congested shallow water model: roof modeling in free surface flow. *ESAIM: Math Mod Num Anal* 2018;52(5):1679–707. doi:[10.1051/m2an/2018032](https://doi.org/10.1051/m2an/2018032).
- [38] Bouchut F, Brenier Y, Cortes J, Ripoll JF. A hierarchy of models for two-phase flows. *J Non Lin Sci* 2000;10(6):639–60. doi:[10.1007/s003320010006](https://doi.org/10.1007/s003320010006).
- [39] Berthelin F. Existence and weak stability for a pressureless model with unilateral constraint. *Math Mod Method App Sci* 2002;12(02):249–72. doi:[10.1142/S0218202502001635](https://doi.org/10.1142/S0218202502001635).
- [40] Berthelin F, Bouchut F. Weak solutions for a hyperbolic system with unilateral constraint and mass loss. In: *Ann. I.H.P. Non Lin. Anal.*; vol. 20. 2003, p. 975–97. doi:[10.1016/S0294-1449\(03\)00012-X](https://doi.org/10.1016/S0294-1449(03)00012-X).
- [41] Chen Z, Zhai X. Global large solutions and incompressible limit for the compressible Navier-Stokes equations. *J Math Fluid Mech* 2019;21(2):26. doi:[10.1007/s00021-019-0428-3](https://doi.org/10.1007/s00021-019-0428-3).
- [42] Cottle RW, Dantzig GB. Complementary pivot theory of mathematical programming. *Lin Alg Appl* 1968;1:103–25. doi:[10.1016/0024-3795\(68\)90052-9](https://doi.org/10.1016/0024-3795(68)90052-9).
- [43] Duvaut G, Lions JL. *Les Inéquations En Mécanique Et Physique*. Paris: Dunod; 1972.
- [44] Bird R, Armstrong RC, Hassager O. *Dynamics of Polymeric Liquids. Volume 1. Fluid Mechanics*. Second ed.; New-York: Wiley; 1987.
- [45] Miller RM, Singh JP, Morris JF. Suspension flow modeling for general geometries. *Chem Eng Sci* 2009;64(22):4597–610. doi:[10.1016/j.ces.2009.04.033](https://doi.org/10.1016/j.ces.2009.04.033).
- [46] Jackson R. *The Dynamics Of Fluidized Particles*. UK: Cambridge University Press; 2000.
- [47] Bouzid M, Izzet A, Trulsson M, Clément E, Claudin P, Andreotti B. Non-local rheology in dense granular flows. revisiting the concept of fluidity. *Eur Phys J E* 2015;38:125. doi:[10.1140/epje/i2015-15125-1](https://doi.org/10.1140/epje/i2015-15125-1).
- [48] Kamrin K. Non-locality in granular flow: Phenomenology and modeling approaches. *Front Phys* 2019;7:116. doi:[10.3389/fphy.2019.00116](https://doi.org/10.3389/fphy.2019.00116).
- [49] Degond P, Tang M. All speed scheme for the low mach number limit of the isentropic euler equations. *Comm Comput Phy* 2011;10(1):1–31. doi:[10.4208/cicp.210709.210610a](https://doi.org/10.4208/cicp.210709.210610a).

- [50] Brezis H, Stampacchia G. Sur la régularité de la solution d'inéquations elliptiques. *Bull S M F* 1968;96:153–80.
- [51] Capriz G, Stampacchia G, editors. *New Variational Techniques In Mathematical Physics*. Springer; 1974.
- [52] Kinderlehrer D, Stampacchia G. *An Introduction To Variational Inequalities And Their Applications*. New York: Academic Press; 1980.
- [53] Fortin M, Glowinski R. *Augmented Lagrangian Methods*. Elsevier; 1983.
- [54] Saramito P. *Efficient C++ Finite Element Computing With Rheolef*. CNRS and LJK; 2018.
- [55] Saramito P. A new brittle-elastoviscoplastic fluid based on the drucker-prager plasticity. *J Non Newt Fluid Mech* 2021;:104584doi:[10.1016/j.jnnfm.2021.104584](https://doi.org/10.1016/j.jnnfm.2021.104584).
- [56] Haddadi H, Shojaei-Zadeh S, Connington K, Morris JF. Suspension flow past a cylinder: particle interactions with recirculating wakes. *J Fluid Mech* 2014;760. doi:[10.1017/jfm.2014.613](https://doi.org/10.1017/jfm.2014.613).
- [57] Oucheggou OA, Pointeau V, Ricciardi G, Guazzelli E, Bergougnoux L. Particle-laden flow around an obstacle in a square pipe: experiments and modeling. *Mech Ind* 2020;21(5):517. doi:[10.1051/meca/2020063](https://doi.org/10.1051/meca/2020063).
- [58] d'Ambrosio E, Blanc F, Lemaire E. Viscous resuspension of non-brownian particles: determination of the concentration profiles and particle normal stresses. *J Fluid Mech* 2021;911. doi:[10.1017/jfm.2020.1074](https://doi.org/10.1017/jfm.2020.1074).
- [59] Roquet N, Saramito P. An adaptive finite element method for Bingham fluid flows around a cylinder. *Comput Meth Appl Mech Engrg* 2003;192(31-32):3317–41. doi:[10.1016/S0045-7825\(03\)00262-7](https://doi.org/10.1016/S0045-7825(03)00262-7).
- [60] Ozenda O. Continuous modelisation of suspension rheology and migration processes. Ph.D. thesis; MSTII UGA; 2019.
- [61] Dbouk T, Lobry L, Lemaire E. Normal stresses in concentrated non-brownian suspensions. *J Fluid Mech* 2013;715:239–72. doi:[10.1017/jfm.2012.516](https://doi.org/10.1017/jfm.2012.516).
- [62] Couturier E, Boyer F, Pouliquen O, Guazzelli E. Suspensions in a tilted trough: second normal stress difference. *J Fluid Mech* 2011;686:26–39. doi:[10.1017/jfm.2011.315](https://doi.org/10.1017/jfm.2011.315).
- [63] Denn MM, Morris JF. Rheology of non-brownian suspensions. *Ann Rev Chem Biomol Eng* 2014;5:203–28. doi:[10.1146/annurev-chembioeng-060713-040221](https://doi.org/10.1146/annurev-chembioeng-060713-040221).

Appendix A. Link with mixture theory

The mixture theory developed by Jackson [46] is based on an asymptotic analysis for small particle radius r_p . Ozenda [60, chap. 2] recently revisited this asymptotic analysis and obtained, at first order in r_p , the following two-velocity system of conservation equations (see also Nott et al. [23]):

$$\left\{ \begin{array}{l} \rho \left(\frac{\partial \mathbf{u}}{\partial t} + \mathbf{u} \cdot \nabla \mathbf{u} \right) - \mathbf{div} (-p_f \mathbf{I} + 2\eta_0 D(\mathbf{u}) + \boldsymbol{\sigma}_h + \boldsymbol{\sigma}_c) = \mathbf{f} \quad (\text{A.1a}) \\ \rho \phi_m \psi \left(\frac{\partial (\mathbf{u} + \mathbf{w})}{\partial t} + (\mathbf{u} + \mathbf{w}) \cdot \nabla (\mathbf{u} + \mathbf{w}) \right) - \mathbf{div} (\boldsymbol{\sigma}_c) - \mathbf{f}_h = 0 \quad (\text{A.1b}) \\ \mathbf{div} \mathbf{u} = 0 \quad (\text{A.1c}) \\ \frac{\partial \psi}{\partial t} + \mathbf{div} ((\mathbf{u} + \mathbf{w}) \psi) = 0 \quad (\text{A.1d}) \end{array} \right.$$

where $\boldsymbol{\sigma}_h$ and $\boldsymbol{\sigma}_c$ denote contributions to the Cauchy stress of the mixture due to hydrodynamic and contact interactions between the particles, respectively, p_f is the fluid phase pressure, and \mathbf{f}_h is the hydrodynamic force exerted on the particle phase.

Present model	Jackson's mixture theory
$\boldsymbol{\sigma}_f$	$\frac{\nu}{2} \langle \boldsymbol{\tau}_l + \boldsymbol{\tau}_l^T \rangle_p$
$\boldsymbol{\sigma}_c$	$\frac{\nu}{2} \langle \boldsymbol{\tau}_c + \boldsymbol{\tau}_c^T \rangle_p$
\mathbf{u}	$\langle \mathbf{u} \rangle$
\mathbf{w}	$\langle \mathbf{u} \rangle_p - \langle \mathbf{u} \rangle$
p_f	$\langle p \rangle_f$
f_h	$\nu \langle f_l \rangle_p$

Table A.6: Correspondence between the notations used in system (A.1) and those used by Jackson [46]. Three different averages are introduced, namely the volume average over the suspension $\langle \cdot \rangle$, the volume average over the fluid phase $\langle \cdot \rangle_f$, and the discrete particle phase average $\langle \cdot \rangle_p$, with ν the number density of particles. See also Ozenda [60, chap. 2].

The correspondence between the notations used in the above system and the different phase averages introduced by Jackson [46] are explained in Table A.6 (see also Ozenda [60, p. 45] for more details). Identifying (2a) with (A.1a), and (2b) with (A.1b), we obtain the following expressions for the Cauchy stress tensor of the mixture and the forces in the particle phase, respectively:

$$-p_f \mathbf{I} + 2\eta_0 D(\mathbf{u}) + \boldsymbol{\sigma}_h + \boldsymbol{\sigma}_c = -p \mathbf{I} + 2\eta_0 D(\mathbf{u}) + \boldsymbol{\tau}_p \quad (\text{A.2a})$$

$$-\mathbf{div} (\boldsymbol{\sigma}_c) - \mathbf{f}_h = -\mathbf{div} (-p_j \mathbf{I} + \boldsymbol{\tau}_p + 2\eta_0 s(\psi) D(\mathbf{w})) + \frac{\eta_0 s(\psi)}{r_p^2} \mathbf{w} \quad (\text{A.2b})$$

The following closure relation can be considered:

$$p_f = p - p_j \quad (\text{A.3a})$$

Then, Equations (A.2a) and (A.2b) successively lead to

$$\begin{aligned}\boldsymbol{\sigma}_h + \boldsymbol{\sigma}_c &= -p_j \mathbf{I} + \boldsymbol{\tau}_p \\ -\mathbf{f}_h + \mathbf{div}(\boldsymbol{\sigma}_h) &= \frac{\eta_0 s(\psi)}{r_p^2} \mathbf{w} - \mathbf{div}(2\eta_0 s(\psi) D(\mathbf{w}))\end{aligned}$$

The first relation corresponds to a classical closure in mixture theory [46, chap. 2], through which the hydrodynamic and contact contributions $\boldsymbol{\sigma}_h$, $\boldsymbol{\sigma}_c$ are lumped into a particle stress, which writes here $-p_j \mathbf{I} + \boldsymbol{\tau}_p$. The second relation writes equivalently:

$$\mathbf{f}_h = -\frac{\eta_0 s(\psi)}{r_p^2} \mathbf{w} + \mathbf{div}(\boldsymbol{\sigma}_h + 2\eta_0 s(\psi) D(\mathbf{w})) \quad (\text{A.3b})$$

This expression identifies term by term with Equation (62) of Nott et al. [23], where the first term on the right-hand side represents the drag force, and the second term is a particle phase hydrodynamic stress. Note that the new corrective term introduced in our model identifies as the difference between the particle phase hydrodynamic stress and the hydrodynamic stress $\boldsymbol{\sigma}_h$ involved in the mixture momentum conservation (A.1a), as discussed by Nott et al. [23]. Since this corrective term is of second-order with respect to r_p , it does not change the overall accuracy of the mixture model.

Appendix B. Poiseuille flow in a long tube

We consider the circular tube geometry represented on Fig. 1, with (r, θ, z) the associated cylindrical coordinate system. This appendix shows how problem (2a)-(2i) reduces asymptotically to problem (3a)-(3j) when tube length L becomes large with respect to its radius R . The flow is assumed to be axisymmetric, i.e. independent upon θ . No-slip conditions are assumed at tube wall i.e. $\mathbf{u}_\Gamma = 0$ in (2g). Moreover, we assume that the initial conditions \mathbf{u}_0 and \mathbf{w}_0 satisfies $u_{0,\theta} = w_{0,\theta} = 0$.

Let U be a characteristic velocity of the mixture and W be a characteristic migration velocity; R/U is then a characteristic time and $\eta_0 U/R$ is a characteristic stress. Dimensionless variables are denoted by tildes, e.g. $\tilde{t} = (U/R)t$, $\tilde{r} = r/R$, $\tilde{z} = z/L$ and $\tilde{\mathbf{u}} = (\tilde{u}_r, \tilde{u}_\theta, \tilde{u}_z) = \mathbf{u}/U$. Finally, let $\xi = R/L$ denote the tube aspect ratio, $\varepsilon = r_p/R$ denote the dimensionless particle radius, and $\zeta = W/U$.

Appendix B.1. Mixture subsystem

Let us first consider the mixture subsystem associated to the unknowns $\tilde{\mathbf{u}}$ and \tilde{p} . Mixture momentum and mass conservations (2a) and (2c) become:

$$\left\{ \begin{array}{l} Re \frac{\tilde{u}_\theta}{\tilde{r}^2} - \frac{\partial_{\tilde{r}}}{\tilde{r}} (\tilde{r} \tilde{\tau}_{p,rr}) + \frac{\tilde{\tau}_{p,\theta\theta}}{\tilde{r}} - \xi \partial_{\tilde{z}} \tilde{\tau}_{p,rz} + \partial_{\tilde{r}} \tilde{p} = 0 \quad (\text{B.1a}) \\ Re (\partial_{\tilde{t}} \tilde{u}_\theta + \xi \tilde{u}_z \partial_{\tilde{z}} \tilde{u}_\theta) - \frac{\partial_{\tilde{r}}}{\tilde{r}^2} (\tilde{r}^2 (\tilde{\tau}_{p,r\theta} + \partial_{\tilde{r}} \tilde{u}_\theta) - \tilde{r} \tilde{u}_\theta) \\ \quad - \xi \partial_{\tilde{z}} (\tilde{\tau}_{p,\theta z} + \xi \partial_{\tilde{z}} \tilde{u}_\theta) = 0 \quad (\text{B.1b}) \\ Re (\partial_{\tilde{t}} \tilde{u}_z + \xi \tilde{u}_z \partial_{\tilde{z}} \tilde{u}_z) - \frac{\partial_{\tilde{r}}}{\tilde{r}} (\tilde{r} (\partial_{\tilde{r}} \tilde{u}_z + \tilde{\tau}_{p,rz})) - \xi \partial_{\tilde{z}} \tilde{\tau}_{p,zz} + \xi \partial_{\tilde{z}} \tilde{p} = 0 \quad (\text{B.1c}) \\ \frac{\partial_{\tilde{r}}}{\tilde{r}} (\tilde{r} \tilde{u}_r) + \xi \partial_{\tilde{z}} \tilde{u}_z = 0 \quad (\text{B.1d}) \end{array} \right.$$

where the Reynolds number is defined by $Re = \rho UR/\eta_0$. For $\xi \rightarrow 0$, relation (B.1d) reduces to $\partial_{\tilde{r}} (\tilde{r} \tilde{u}_r) = 0$. Hence, the boundary condition (2g) yields $\tilde{u}_r(\tilde{t}, \tilde{r}=0) = \tilde{u}_r(\tilde{t}, \tilde{r}=1) = 0$ at any time $\tilde{t} \in]0, \tilde{T}[$. Thus, $\tilde{u}_r = 0$ at any time. Moreover, since we assume $\tilde{u}_\theta = 0$ at $\tilde{t} = 0$, from (B.1b), this identity remains true at any time. Thus $\tilde{\mathbf{u}} = (0, 0, \tilde{u}_z)$.

Observe in (B.1a) that the term $\partial_{\tilde{r}} \tilde{\tau}_{p,rr}$, responsible for the migration, appears at the same order in ξ as the pressure derivative $\partial_{\tilde{r}} \tilde{p}$. Conversely, in (B.1c), the term $\xi \partial_{\tilde{z}} \tilde{p}$ should be at zeroth order in ξ ; otherwise the suspension would not move in a long tube when $\xi \rightarrow 0$. Finally, the pressure is assumed to admit the following expansion in ξ :

$$\tilde{p}(\tilde{t}, \tilde{r}, \tilde{z}) = \xi^{-1} \tilde{f}_z(\tilde{t}) \tilde{z} + \tilde{p}_0(\tilde{t}, \tilde{r}) + \mathcal{O}(\xi)$$

where \tilde{f}_z depends only upon \tilde{t} , and \tilde{p}_0 depends upon \tilde{t} and \tilde{r} but is independent of \tilde{z} , as inferred from (B.1a). Then, for $\xi \rightarrow 0$, momentum conservation (B.1a) and (B.1c) reduce to

$$-\frac{\partial_{\tilde{r}}}{\tilde{r}} (\tilde{r} \tilde{\tau}_{p,rr}) + \frac{\tau_{p,\theta\theta}}{\tilde{r}} + \partial_{\tilde{r}} \tilde{p}_0 = 0 \quad (\text{B.2a})$$

$$Re \partial_{\tilde{t}} \tilde{u}_z - \frac{\partial_{\tilde{r}}}{\tilde{r}} (\tilde{r} (\partial_{\tilde{r}} \tilde{u}_z + \tilde{\tau}_{p,rz})) + \tilde{f}_z = 0 \quad (\text{B.2b})$$

Two types of controls can be considered for the flow of the mixture: either the pressure drop \tilde{f}_z or the flow rate can be imposed. Here, we choose to impose the flow rate, denoted by q . The characteristic mixture velocity is then defined as $U = 2q/(\pi R^2)$, which is equal to twice the average velocity, such that the dimensionless flow rate expresses as

$$\int_0^1 \tilde{u}_z(\tilde{t}, \tilde{r}) \tilde{r} d\tilde{r} = \frac{1}{4} \quad (\text{B.2c})$$

and \tilde{f}_z in (B.2b) interprets as a Lagrange multiplier for the imposition of the flow rate constraint (B.2c). Note that when $\psi = 0$, from (2f), the particle stress τ_p vanishes, the fluid is Newtonian and U coincides with the maximal value of the mixture velocity.

Appendix B.2. Congested subsystem

Let us now turn to the congested subsystem associated to the unknowns $\tilde{\mathbf{w}}$, \tilde{p}_j and ψ . Since $\tilde{w}_\theta = 0$ at $t=0$, we assume that $\tilde{\mathbf{w}} = (\tilde{w}_r, 0, \tilde{w}_z)$ at any time. Note that $\tilde{w}_r \neq 0$ in general, since the particles are expected to migrate in the tube. The momentum and mass conservations of the particle phase (2b) and (2d) become:

$$\left\{ \begin{array}{l} Re \phi_m \psi (\zeta \partial_{\tilde{t}} \tilde{w}_r + \zeta^2 (\tilde{w}_r \partial_{\tilde{r}} \tilde{w}_r + \xi \tilde{w}_z \partial_z \tilde{w}_r) + \xi \zeta \tilde{u}_z \partial_z \tilde{w}_r) \\ \quad + \varepsilon^{-2} \zeta s(\psi) \tilde{w}_r - \zeta \frac{\partial_{\tilde{r}}}{\tilde{r}} (2\tilde{r} s(\psi) \partial_{\tilde{r}} \tilde{w}_r) - \xi \zeta \partial_z (s(\psi) (\partial_{\tilde{r}} \tilde{w}_z + \xi \partial_z \tilde{w}_r)) \\ \quad + \partial_{\tilde{r}} \tilde{p}_j = \frac{\partial_{\tilde{r}}}{\tilde{r}} (\tilde{r} \tilde{\tau}_{p,rr}) - \frac{\tilde{\tau}_{p,\theta\theta}}{\tilde{r}} + \xi \partial_z \tilde{\tau}_{p,rz} \\ Re \phi_m \psi (\partial_{\tilde{t}} \tilde{u}_z + \zeta \partial_{\tilde{r}} \tilde{w}_z + \zeta^2 (\tilde{w}_r \partial_{\tilde{r}} \tilde{w}_z + \xi \tilde{w}_z \partial_z \tilde{w}_z) + \xi \zeta \tilde{u}_z \partial_z \tilde{w}_z) \\ \quad + \varepsilon^{-2} \zeta s(\psi) \tilde{w}_z - \zeta \frac{\partial_{\tilde{r}}}{\tilde{r}} (\tilde{r} s(\psi) (\partial_{\tilde{r}} \tilde{w}_z + \xi \partial_z \tilde{w}_r)) - \xi^2 \zeta \partial_z (2s(\psi) \partial_z \tilde{w}_z) \tilde{p}_j \\ \quad + \xi \partial_z = \frac{\partial_{\tilde{r}}}{\tilde{r}} (\tilde{r} \tilde{\tau}_{p,rz}) + \xi \partial_z \tilde{\tau}_{p,zz} \\ \partial_{\tilde{t}} \psi + \zeta \frac{\partial_{\tilde{r}}}{\tilde{r}} (\tilde{r} \tilde{w}_r \psi) + \xi \tilde{u}_z \partial_z \psi + \xi \zeta \partial_z (\tilde{w}_z \psi) = 0 \end{array} \right.$$

By passing to the limit $\xi \rightarrow 0$ and neglecting second-order terms in ζ , which are associated to inertia effects, the previous system becomes:

$$\left\{ \begin{array}{l} Re \zeta \phi_m \psi \partial_{\tilde{t}} \tilde{w}_r + \varepsilon^{-2} \zeta s(\psi) \tilde{w}_r - \zeta \frac{\partial_{\tilde{r}}}{\tilde{r}} (2\tilde{r} s(\psi) \partial_{\tilde{r}} \tilde{w}_r) + \partial_{\tilde{r}} \tilde{p}_j \\ \quad = \frac{\partial_{\tilde{r}}}{\tilde{r}} (\tilde{r} \tilde{\tau}_{p,rr}) - \frac{\tilde{\tau}_{p,\theta\theta}}{\tilde{r}} \end{array} \right. \quad (\text{B.3a})$$

$$\left\{ \begin{array}{l} Re \phi_m \psi (\partial_{\tilde{t}} \tilde{u}_z + \zeta \partial_{\tilde{r}} \tilde{w}_z) + \varepsilon^{-2} \zeta s(\psi) \tilde{w}_z - \zeta \frac{\partial_{\tilde{r}}}{\tilde{r}} (\tilde{r} s(\psi) \partial_{\tilde{r}} \tilde{w}_z) \\ \quad = \frac{\partial_{\tilde{r}}}{\tilde{r}} (\tilde{r} \tilde{\tau}_{p,rz}) \end{array} \right. \quad (\text{B.3b})$$

$$\left\{ \begin{array}{l} \partial_{\tilde{t}} \psi + \zeta \frac{\partial_{\tilde{r}}}{\tilde{r}} (\tilde{r} \tilde{w}_r \psi) = 0 \end{array} \right. \quad (\text{B.3c})$$

Appendix B.3. System closure

Finally, let us turn to the expression of particle stress tensor $\boldsymbol{\tau}_p$ given by (2f). Since $\tilde{\mathbf{u}}(\tilde{t}, \tilde{r}) = (0, 0, \tilde{u}_z(\tilde{t}, \tilde{r}))$, the norm of the strain rate writes $|2\tilde{D}(\tilde{\mathbf{u}})| = |\partial_{\tilde{r}} \tilde{u}_z|$ and the components of $\boldsymbol{\tau}_p$ express as explicit relations involving \tilde{u}_z and ψ , as shown by (4).

The final system involves seven equations, namely (B.2a)-(B.2c), (B.3a)-(B.3c), and (1), and seven unknowns: \tilde{u}_z , \tilde{p}_0 , \tilde{f}_z , \tilde{w}_r , \tilde{w}_z , \tilde{p}_j , and ψ . All these unknowns depend both upon time \tilde{t} and radial position \tilde{r} , except for \tilde{f}_z that only depends upon time. Observe that Equation (B.2a) leads to an explicit computation of \tilde{p}_0 ,

and is used in post-treatment to obtain a first order approximation in ξ of mixture pressure \tilde{p} . Similarly, \tilde{w}_z appears only in equation (B.3b); consequently, this equation can be integrated explicitly after the resolution of the five remaining equations. The system is closed by suitable initial and boundary conditions, and is summarised in (3). Finally note that, for convenience, tilde notations are dropped in the main text (section 2.2), and the two-velocities $\tilde{\mathbf{u}}$ and $\tilde{\mathbf{w}}$ are normalised by the same characteristic velocity U .

Appendix C. Uzawa algorithm

Problem (O), as defined in subsection 3.2, is solved by minimising the cost function J defined by equation (12). Let us introduce the dual function J^* defined for all $q \in L^2$ by:

$$J^*(q) = - \min_{(v, \xi) \in H_0^1 \times L^2} L(v, \xi ; q)$$

The problem writes equivalently as a minimisation problem for this dual function:

$$p_j = \arg \min_{q \in L^2} J^*(q)$$

The numerical procedure used to solve this problem, based on Uzawa method, is described in subsection B.1, with two technical lemmas gathered in subsection B.2.

Appendix C.1. Numerical algorithm

The Uzawa algorithm for the augmented Lagrangian method expresses as a constant-step descent algorithm for the dual function J^* :

- $m = 0$: let $p_j^{(0)}$ be given.
- $m \geq 1$: let $p_j^{(m-1)}$ be known. Then compute:

$$p_j^{(m)} = p_j^{(m-1)} - \mu \nabla J^* \left(p_j^{(m-1)} \right).$$

Here, $m \in \mathbb{N}$ denotes the descent loop index, which is implemented as an inner loop inside the fixed point loop with index k introduced in subsection 3.1. A numerical parameter m_{max} is introduced, such that the stopping criterion for this inner loop is defined as $m > m_{max}$. Note that the constant-descent step has been chosen equal to the augmentation parameter μ . Note also that J^* is differentiable. Then, expanding its gradient, we obtain an equivalent formulation of the descent algorithm:

- $m = 0$: let $p_j^{(0)}$ be given.

- $m \geq 1$: let $p_j^{(m-1)}$ be known. Then compute successively:

$$\begin{aligned} (w_r^{(m)}, \delta^{(m)}) &= \arg \min_{(v, \xi) \in H_0^1 \times L^2} L(v, \xi; p_j^{(m-1)}) \\ p_j^{(m)} &= p_j^{(m-1)} + \mu (\delta^{(m)} - Bw_r^{(m)}) \end{aligned}$$

To simplify the simultaneous minimisation versus (v, ξ) of the Lagrangian, the algorithm is modified by decoupling the first step as:

- $m = 0$: let $p_j^{(0)}$ and $\delta^{(0)}$ be given.
- $m \geq 1$: let $p_j^{(m-1)}$ and $\delta^{(m-1)}$ be known. Then compute successively:

$$\begin{aligned} w_r^{(m)} &= \arg \min_{v \in H_0^1} L(v, \delta^{(m-1)}; p_j^{(m-1)}) \\ \delta^{(m)} &= \arg \min_{\xi \in L^2} L(w_r^{(m)}, \xi; p_j^{(m-1)}) \\ p_j^{(m)} &= p_j^{(m-1)} + \mu (\delta^{(m)} - Bw_r^{(m)}) \end{aligned}$$

From (12), the Lagrangian L is quadratic and differentiable versus v . Thus, the first step of the above algorithm reduces to a linear sub-problem, namely, find $w_r^{(m)} \in H_0^1$ such that, for all $v \in H_0^1$, we have

$$\frac{\partial L}{\partial v}(w_r^{(m)}, \delta^{(m-1)}, p_j^{(m-1)}) = 0$$

The Lagrangian L is both nonlinear and non-differentiable versus ξ , but involves a sub-differential with respect to ξ . Hence, the optimal value $\delta^{(m)}$ verifies $0 \in \partial_\xi L(w_r^{(m)}, \delta^{(m)}, p_j^{(m-1)})$, where $\partial_\xi L(w_r^{(m)}, \delta^{(m)}, p_j^{(m-1)})$ is the sub-differential of L with respect to the variable ξ . The second step of the descent algorithm is then solved locally. The sub-gradient of the indicator of $[g(r), \infty[$, denoted $\partial \mathbb{I}_{[g(r), \infty[}$, verifies, for all $\xi \in \mathbb{R}$:

$$\partial \mathbb{I}_{[g(r), \infty[}(\xi) = \begin{cases} \emptyset & \text{when } \xi < g(r) \\ [0, \infty[& \text{when } \xi = g(r) \\ \{0\} & \text{otherwise} \end{cases}$$

For all $r \in [0, 1]$, the second step then expresses:
find $\delta^{(m)}(r) \in \mathbb{R}$ such that:

$$\begin{aligned} &0 \in \partial \mathbb{I}_{[g(r), \infty[}(\delta^{(m)}(r)) + p_j^{(m-1)}(r) + \mu \delta^{(m)}(r) - \mu Bw_r^{(m)}(r) \\ \iff &\begin{cases} \delta^{(m)}(r) > g(r) & \text{and } \delta^{(m)}(r) = Bw_r^{(m)}(r) - \frac{p_j^{(m-1)}(r)}{\mu} \\ \text{or} \\ \delta^{(m)}(r) = g(r) & \text{and } \delta^{(m)}(r) \geq Bw_r^{(m)}(r) - \frac{p_j^{(m-1)}(r)}{\mu} \end{cases} \end{aligned}$$

Finally, the computation of $\delta^{(m)}$ reduces to an explicit relation, as shown in [Appendix C.2](#) (lemma 1), and the practical Uzawa algorithm writes:

- $m = 0$: let $p_j^{(0)}$ and $\delta^{(0)}$ be given.
- $m \geq 1$: let $p_j^{(m-1)}$ and $\delta^{(m-1)}$ be known. Then successively:
 - i) find $w_r^{(m)} \in H_0^1$ such that, for all $v \in H_0^1$, we have

$$\begin{aligned} a(w_r^{(m)}, v) + \mu \int_0^1 B w_r^{(m)} B v r \, dr \\ = \ell(v) + \int_0^1 \left(p_j^{(m-1)} + \mu \delta^{(m-1)} \right) B v r \, dr \end{aligned} \quad (\text{C.1a})$$

- ii) compute explicitly:

$$\delta^{(m)} = \max \left(g, B w_r^{(m)} - \frac{p_j^{(m-1)}}{\mu} \right) \quad (\text{C.1b})$$

$$p_j^{(m)} = p_j^{(m-1)} + \mu \left(\delta^{(m)} - B w_r^{(m)} \right) \quad (\text{C.1c})$$

This algorithm has been shown to converge for any $\mu > 0$ [[53](#), theorem 5.1]). Recall that the solution is independent upon μ . At convergence, [\(C.1c\)](#) leads to $\delta = B w_r$ and then [\(C.1a\)](#) is exactly a weak formulation of [\(11a\)](#). Since $w_r \in H_0^1$ in [\(C.1a\)](#), we also obtain [\(11c\)](#). Replacing $\delta = B w_r$ in [\(C.1b\)](#), we obtain

$$B w_r = \max \left(g, B w_r - \frac{p_j}{\mu} \right)$$

which leads to [\(11b\)](#), as shown in [Appendix C.2](#) (lemma 2). Thus, the previous algorithm effectively provides a solution of [\(11a\)](#)-[\(11c\)](#).

Appendix C.2. Technical lemmas

Lemma 1. *With the notations defined in section 3, we state the following equivalence relation:*

$$\delta^{(m)} = \max \left(g, B w_r^{(m)} - \frac{p_{c,0}^{(m-1)}}{\mu} \right) \iff \begin{cases} \delta^{(m)} > g \text{ and } \delta^{(m)} = B w_r^{(m)} - \frac{p_j^{(m-1)}}{\mu} \\ \text{or} \\ \delta^{(m)} = g \text{ and } \delta^{(m)} \geq B w_r^{(m)} - \frac{p_j^{(m-1)}}{\mu} \end{cases}$$

Proof. The maximum condition is split between two cases that are equivalent to the right hand side disjunctive relation in lemma 1:

$$\begin{cases} \delta^{(m)} = g \\ g \geq Bw_r^{(m)} - \frac{p_j^{(m-1)}}{\mu} \end{cases} \iff \begin{cases} \delta^{(m)} = g \\ \delta^{(m)} \geq Bw_r^{(m)} - \frac{p_j^{(m-1)}}{\mu} \end{cases}$$

$$\begin{cases} \delta > g \\ \delta = Bw_r^{(m)} - \frac{p_j^{(m-1)}}{\mu} \end{cases} \iff \begin{cases} \delta = Bw_r^{(m)} - \frac{p_j^{(m-1)}}{\mu} \\ g < Bw_r^{(m)} - \frac{p_j^{(m-1)}}{\mu} \end{cases}$$

□

Lemma 2. *With the notations defined in section 3, we state*

$$Bw_r = \max\left(g, Bw_r - \frac{p_j}{\mu}\right) \implies g \leq Bw_r \perp p_j \geq 0$$

Proof.

$$Bw_r = \max\left(g, Bw_r - \frac{p_j}{\mu}\right) \implies \begin{cases} Bw_r \geq g \\ Bw_r \geq Bw_r - \frac{p_j}{\mu} \end{cases}$$

- The condition $Bw_r \geq g$ is evidently satisfied.
- Recalling $\mu > 0$, the positivity of p_j is deduced :

$$Bw_r \geq Bw_r - \frac{p_j}{\mu} \implies p_j \geq 0$$

- The condition $p_j (Bw_r - g) = 0$ is finally stated:

$$p_j > 0 \implies Bw_r - \frac{p_j}{\mu} < Bw_r \implies Bw_r = g$$

$$Bw_r > g \implies Bw_r - \frac{p_j}{\mu} = Bw_r \implies p_j = 0$$

Hence the unilateral condition $g \leq Bw_r \perp p_j \geq 0$ is stated.

□

Appendix D. Identification of the rheological parameters

Steady state flow profiles computed with our model show a very low sensitivity to the values of rheological parameters K_n , λ_2 , λ_3 and α . Hence, only the value of K_s was adjusted to fit with the migration data of Oh et al. [18] (see Fig. 8). Values of λ_2 and λ_3 define the relative magnitude of the normal stress

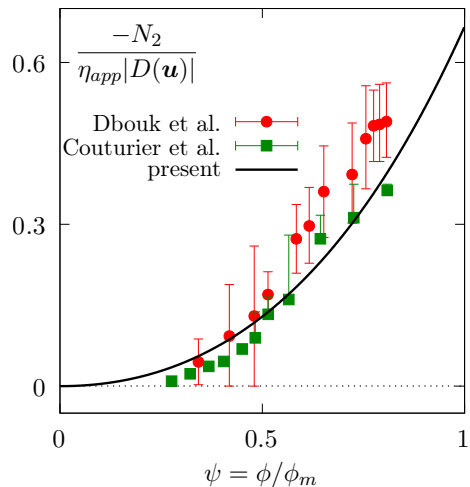


Figure D.9: Steady-state normal stress ratio $N_2/\eta_{app}|2D(\mathbf{u})|$ as a function of reduced volume fraction ψ : comparison between the predictions the rheological model (with values indicated in table 2 and $\phi_m = 0.60$) and experimental data of Dbouk et al. [61] and Couturier et al. [62].

differences $N_1 = \tau_{p,zz} - \tau_{p,rr}$ and $N_2 = \tau_{p,rr} - \tau_{p,\theta,\theta}$. The values chosen for these parameters (see table 2) ensure that $|N_2| > 3|N_1|$, in agreement with experimental observations [63]. The value of K_n controls the magnitude of the ratio $N_2/\eta_{app}|2D(\mathbf{u})|$, and was set to fit with experimental data from Dbouk et al. [61] and Couturier et al. [62], as shown on Fig. D.9. Finally, the parameter α should verify $\alpha \in [2, 5]$, see Miller and Morris [25]. The present choice $\alpha = 3$ corresponds to an intermediate value. We observed that the smaller the value of α , the faster the system reaches the steady state regime.